Politecnico di Torino

Corso di Laurea Magistrale in Petroleum and Mining Engineering
A.a. 2021/2022

Synthesis and Optimization of MOF Catalyst for Biomass Valorization

Application on MOF-808

Supervisors:
Professor Serena Esposito
Dr. Olimpia Tammaro

Author:
Mohammad Jawad Younes
s287294

In dedica a

Serena e Olimpia per il loro supporto e guida durante il lavoro.

Contents

List of Figures

List of Tables

LIST OF ABBREVIATIONS AND ACRONYMS

MOF: Metal-Organic Framework

SBU: Secondary Building Unit

DMF: N,N Dimethyl formamide

BTC: Trimesic acid

XRD: X-Ray Diffraction

TGA: Thermo-gravimetric Analysis

BET: Brunauer-Emmett-Teller

NMR: Nuclear Magnetic Resonance

SEM: Scanning Electron Microscope

LA: Levulinic Acid

ML: Methyl Levulinate

EL: Ethyl Levulinate

AF: Formic Acid

AA: Acetic Acid

$ZrOCl_2.8H_2O$: Zirconium(IV) oxychloride octahydrate

$ZrCl_4$: Zirconium(IV) Chloride

Abstract

The gradual depletion of fossil fuels accompanied by environmental hazards has triggered more studies toward the development of renewables. Biomass is a great candidate endowed by its affordability, availability, and zero CO_2 emissions.

Different biomass platform molecules contribute to the production of many crucial chemicals used in our everyday life. Methyl Levulinate is one of the important molecules that contribute to the development of many fields such as fuel additives, coatings, adhesives, and plasticizers. However significant efforts are recommended to design suitable catalytic processes that can increase the material and energy efficiency of biomass reactions.

Metal-Organic Frameworks consisting of metal clusters bridged with organic ligands form well-ordered highly crystalline materials, with nano-pore size distribution giving rise to the ultrahigh surface area, permanent porosity, tunable pore size, and unsaturated coordination sites that provide additional improvements to the catalytic activity of such materials over zeolites.

Although the literature study is intensive regarding MOF, a systematic analysis of the synthesis process itself and of the effect of the different variables that intervene in it are rather scarce. Therefore, the objective of this paper is to rigorously assess the intrinsic effect of the use of different synthetic approaches and assess the direct effect of varying parameters on the chemical and physical properties of the synthesized MOF, followed by a study of these different characteristics on the yield of the reaction.

Chapter 1 Transition to Biomass

1.1 Fossil Fuels

In our modern society, non-renewables such as petroleum, gas, and coal are main energy resources that contribute to our technological development and the supply of diverse set of chemicals.

However, these nonrenewable resources will not be reproduced again during our life span due to the complexity and longevity of the chemical reactions involved in their decomposition, the specificity of the geological typologies needed to be trapped, and the presence of right conditions from pressure, temperature and lack of oxygen. These resources are experiencing a decline in their reserves worldwide, mainly due to natural reasons.

Carbon dioxide considered as the primary greenhouse responsible for most of pollution emissions. Resulting from exploitation of fossil fuels and violations of forestry and other land use, these gases absorb solar energy and keep heat closer to earth's surface.[1]

1.2 Alternatives to Fossil Fuels

With the exponential human growth, depletion of fossil fuels, and deterioration of the environment, alarming procedures have to be done to replace the high dependency on fossil fuels with more renewable resources. New energy sources such as solar, wind, tidal, geothermal, controllable nuclear fusion, and biomass energy have attracted attention. However, the limited time characteristics of solar and wind energy make these energy sources uncertain, and the localization characteristics of tidal and geothermal energy prevent these energy sources from being widely used. Moreover, energy generated from controllable nuclear fusion is still under study and testing before we can truly use it to serve humanity. It also has to overcome high costs and concerns about nuclear waste disposal[2].

To sum up, these resources can work locally, but they cannot secure a global energy production aligned with the growing energy demand. We have to look for a widely spread and tradable resource that can be treated easily for the generation of our energy needs.

1.2.1 Biomass is the solution

Bioenergy remains the best resource candidate that helps to meet our energy demands. It is a form of renewable energy derived from living organic materials which can be used to produce transportation fuels, heat, electricity, and products[3].

The use of biomass produces an insignificant amount of CO_2, the same amount that was absorbed by the plants completing this so-called ''carbon cycle''. In other words, if biomass is continuously used, there will be relatively no increment in the total volume of CO_2 in the atmosphere leading to the ''carbon neutrality''[4].

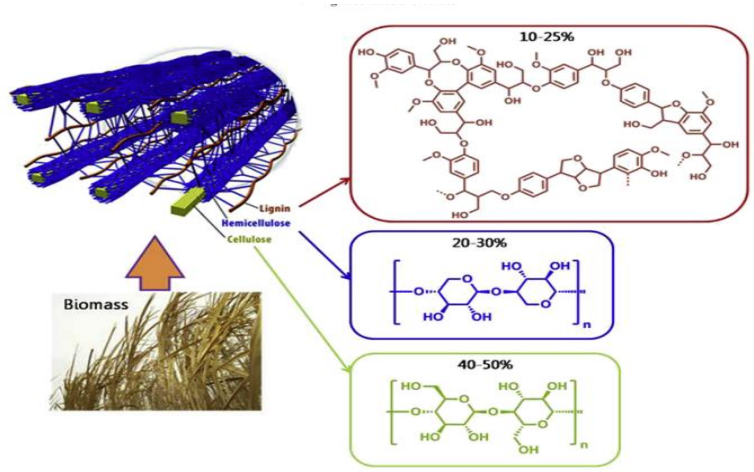

Figure 1.1: Components of Lignocellulose

Lignocellulose, the most abundant form of biomass is composed of three primary components with different percentages as shown in Figure 1.1; cellulose (40–50 wt%), hemicellulose (25–30 wt%), and lignin (15–30 wt%) [5].

1.2.2 Platform Molecules

Valorization of biomass starts with the hydrolysis of cellulose and to efficiently produce hexoses and pentoses. Then they are followed by different reactions of pyrolysis, hydrolysis, condensation, isomerization, deoxygenation, hydrogenation, and oxidation to obtain precious chemical products ranging from C1-C6[6].

Platform molecules, referred to as the building block chemical derived from the processing of biomass residues, are highly functionalized; contain several functional groups that can help in processing them into different value-added final products. In addition, they are highly oxygenated, in contrast to petroleum-based feed-stocks, which allows for more efficient and lower-cost refinery processes. The poor oxygenation of petroleum-based products requires higher energy processes accompanied by metal catalysts such as lead and chromium that are usually disposed of in the environment after regeneration several times[4].

1.2.3 Levulinic Acid

Levulinic acid, known as 4-isovaleric acid or 4-oxopentanoic acid, with molecular formula $C_5H_8O_3$[7], is a renewable compound obtained from the cracking of lignocellulosic biomass feedstock[8]. It possesses the carboxyl and the ketone group, making it a versatile compound

with different reaction pathways and final products as shown in Figure 1.2[9]. It can undergo various chemical reactions. It is an important starting material for bio-renewable fuels, biodegradable herbicides, and photosynthesis promoters. Many derivatives can be obtained from LA due to its highly functionalized molecule[10].

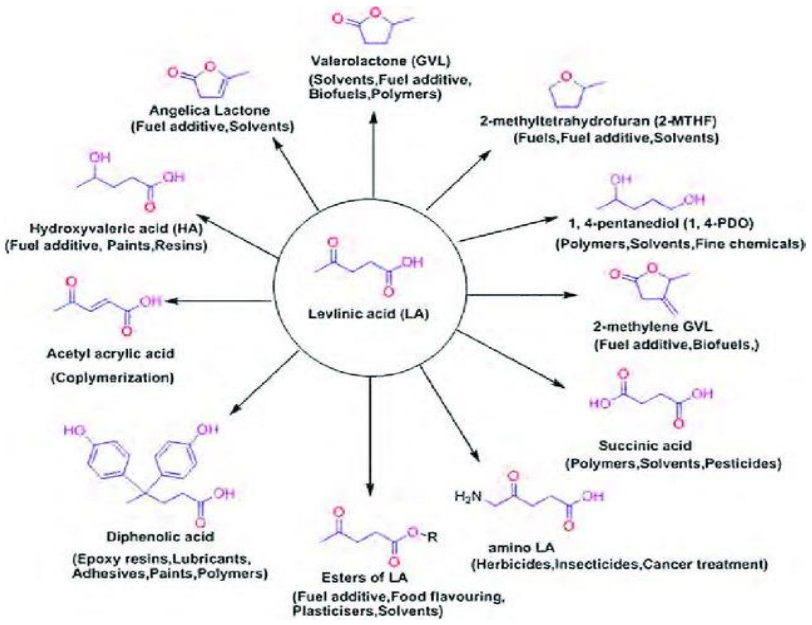

Figure 1.2: Levulinic Acid Derivatives

Alkyl Levulinates are essential gasoline additives due to their high octane number, lubricity, solubility, and volatility. Also, they can be used as flavoring compounds and plasticizers. Ethyl levulinate is used as an oxygenated diesel additive up to 20% content that increases engine efficiency. It's also characterized by good energy content and high lubricity and flash point, which renders it suitable for gasoline blendstock[8]. Methyl levulinate is a vital molecule derived from LA due to its unique physical and chemical properties that renders it useful in many sectors. Moreover, Alkyl Levulinates prepared from esterification of levulinic acid as raw material are considered green solvents since they are environmentally friendly and have a lower boiling point[2].

1.3 Biomass Catalytic Reactions

The transformation of the biomass into platform molecules and into other valuable chemical products requires the presence of catalysts characterized by well-developed catalytic properties such as high surface area, well-ordered structure, and dual acidic sites.

Both homogenous and heterogeneous were developed for the treatment of biomass feed-stocks. However, another challenge associated with homogenous catalysts is the lack of selectivity toward the final desirable products because the interaction between the substrate and the catalysis is more challenging to control. Besides, other processes such as separation

and purification render homogenous catalysts less attractive and even more complex and costly at the industrial level[11]. Nevertheless, homogenous catalysts usually suffer from toxic metals, strong corrosivity, severe pollution, and poor recyclability, making it sometimes more complicated to meet the increasingly strict environmental regulations[12].

That said, heterogeneous catalysts with active sites can be an efficient solution for providing reliable catalyst durability and convenient product isolation. Moreover, tunable composition, morphology, and porous architecture endows capabilities for heterogeneous catalysts. In addition, the high surface areas of heterogeneous catalysts are beneficial for the enrichment and exposure of active sites, allowing their accessibility and utilization. Furthermore, the large pores, as well as channels, would also facilitate and control the mass diffusion and sorption and, to some extent, modify the product selectivity through steric effects. Bi-functionality, primarily as Bronsted-Lewis acid sites is also a feature that the catalyst must attain since most of the biomass reactions occurs in a cascade manner, wherein in each reaction, a specific site/functional group is targeted[11].

Although some success has been achieved by solid catalysts such as zeolites, metal oxides, and acidic resins, their usage in bio-mass valorization is still limited due to the relatively low development of their catalytic properties such as the surface area or accurate detection of active sites[13].The modern class of the hybrid nano-porous inorganic-organic materials(MOFs) are now being the most studied solids in heterogeneous catalysis as they almost entirely fit these requirements thanks to their intrinsic compositional, structural, and physicochemical properties, which can be rationally designed[14].

Chapter 2 The MOF

2.1 Introduction to MOF

They are formed by periodic arrangement between inorganic nodes that are the metal clusters and the bridging organic ligands. These linkers are bonded to the metals through a pair of electron donors that is usually a carboxylate oxygen atom or nitrogen atoms[15]. The combination between the nodes and the linkers can result in 1-D chains, 2-D sheets, and 3-D networks. The general synthesis approach is shown in Figure 2.1[16].

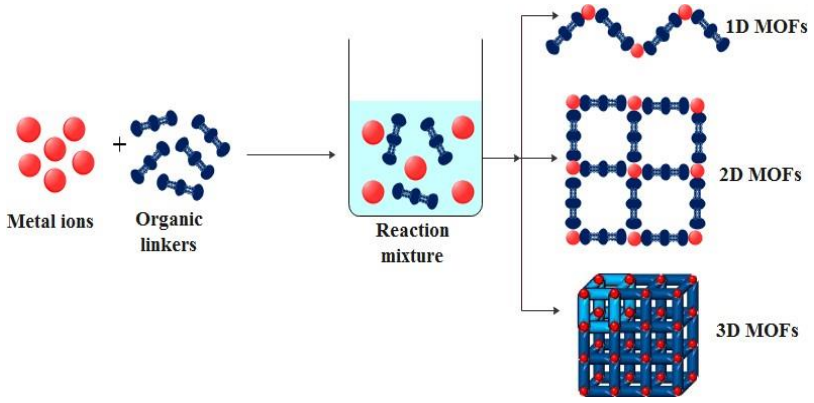

Figure 2.1: MOF Synthesis Strategy

In general, two secondary building units are involved in the synthesis of the MOF structure. The first SBU is determined as the organic linker, which can have several number of coordination numbers. The organic linker is usually composed of carboxylates, phosphonate, or sulfonate ions. They act as a bridge between two metal centers that enable the formation of a 3D framework. The different typologies and connection numbers of the organic ligands are shown in Figure 2.2[17].

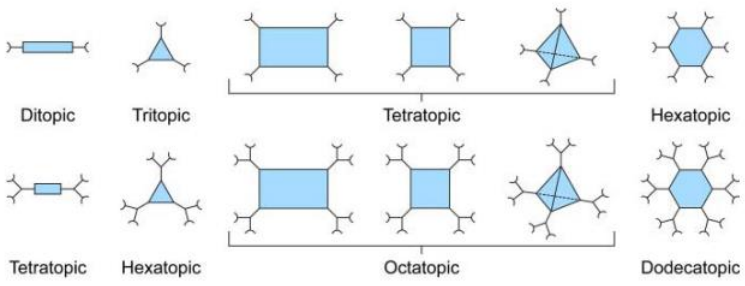

Figure 2.2: Types of Organic Ligands

The second SBU is the metal atom, a finite polyatomic inorganic cluster with two or more metal atoms or an infinite inorganic unit such as an infinite periodic rod of metal atom[18]. The metal ion and its oxidation state play an important role in determining the coordination geometry, the number of charge balancing ligands, and the preferred coordination determined by the hard/soft, acid/base consistency[19]. Also, several geometries of the cluster can result from these parameters as square planar (four coordination) and octahedral (six coordination).

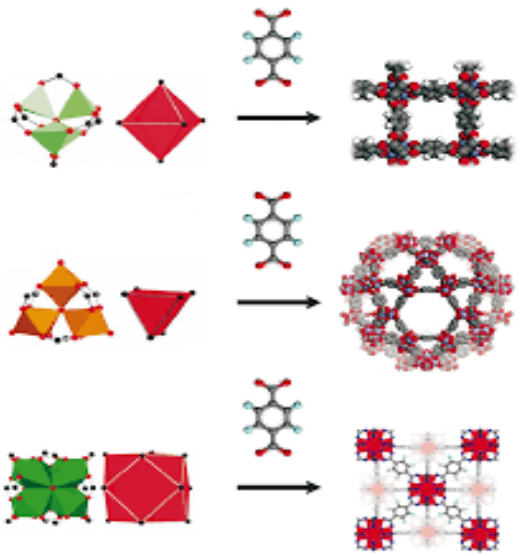

Figure 2.3: MOFs obtained from different metallic clusters but same organic ligand

The final typology is determined by both SBUs governed by the nodal connectivity, orientation, cluster typology, ligand used, or solvent used. This richness in the MOFs typologies is referred to the diverse geometries of metal clusters and several coordination extensions of the organic ligands[20]. Thus, there are an inordinate number of theoretical MOFs due to the enormous diversity of metal ions and bridging organic ligands that can be combined[21] as seen in Figure 2.3[22].

The unique structural topologies, great surface area, ultra-high porosity, and tunable pore size, shape, and network can be tailored to fit many specific applications[23]. Also, the different constituents of MOF are connected by relatively weak bonds (pi bonds, Van der Waals, or Hydrogen bonds), which give the structure higher flexibility than its crystalline structure.

2.2 Stability of a MOF

Chemical stability: Can be assessed by the treatment of the material with different liquid and gaseous chemicals, followed by XRD analysis to check if the material has been altered or degraded.

Thermal stability: Can be assessed by thermo-gravimetric analysis (TGA) or differential scanning calorimetry (DSC), where a mass loss is registered upon heating the material, indicating the decomposition or alteration of the structure.

Mechanical stability: It is done with similar techniques used in material science studies, such as compression, and nano-indentation for the determination of Young modulus, and tensile strength[17].

2.3 Applications of MOF

MOFs are valuable materials for the refinement of traces of the substance from different gases. MOFs can be utilized in stripping ppm levels of sulfur from different flue gases. The high surface, adjustable pores, and controllable surface properties make MOFs perfect candidates for gas separation. For example, they can be used to remove CO_2 and CH_4 from natural gas upon treatment in gas refineries[24].

The porous crystallite structure of MOFs allows them to absorb, contain and release compounds. They can be used to purify seawater from salt and chemicals to provide clean water for drinking. MOF technology is also used in mining to mitigate waste and recover valuable metals[25].Different uses are mentioned in Figure 2.4[26]

Figure 2.4: Uses of MOF

The main application of interest is the catalytic activity of MOF that is achieved by its highly ordered arrangement and porosity structure that allows the transport of reactants and products through the catalytic sites. In addition, the tunable chemical functionality endows it as a candidate for many catalytic transformations. Several structural features of MOFs can be harvested for catalytic applications as also shown in Figure 2.5[27]:

(1) by using the metal nodes of the material when coordination vacancies are available

(2) by using the linker as an organo-catalytic site or via post-synthetic modification

(3) as hosts for the encapsulation of additional catalytic sites such as nanoparticles, enzymes, or other moieties[28].

Metal atoms are partially connected to solvent molecules that are removed upon elevated heating and open the void space into more desirable molecules. Leaving these metal clusters coordinatively unsaturated increases the gas uptake of the MOF, especially for gases such as H_2, CO_2, and CH_4. Also, the uncoordinated cation metals are considered as sites for Bronsted Acid sites, which is important for a wide range of Biomass reactions. Post synthetic modification (PSM) works on introducing new functional groups to the linkers that serve as catalytic sites for some reactions.

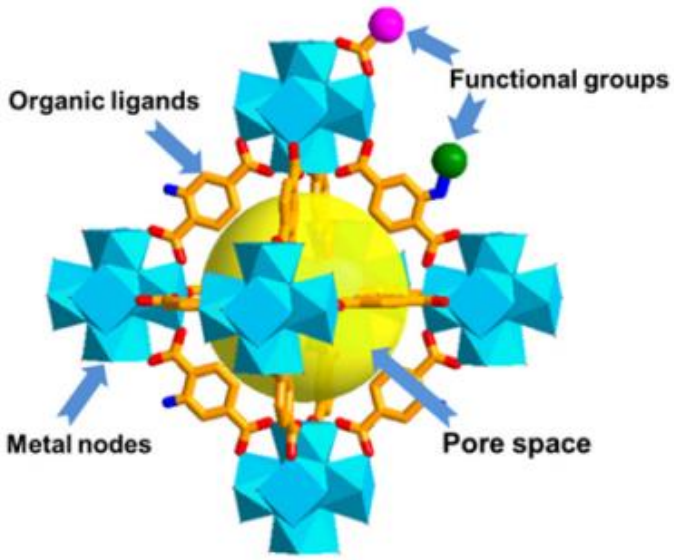

Figure 2.5: Active sites in a MOF

2.4 Synthesis of MOF

Solvothermal methods are usually the most widespread method for preparing MOFs via conventional electric heating at a controlled temperature. Generally, high solubility organic solvents, such as DMF, DEF, acetone, ethanol, methanol, or acetonitrile are used.

Hydrothermal methods are almost the same procedures; however, as its name shows, water is used instead of the initial solvents for an environmental approach that substitutes the use of organic solvents.

The slow evaporation method takes place at room temperature. However, this results in a significantly longer reaction time than other methods. In this synthesis, the initial solution is progressively concentrated by the slow evaporation of the solvent.

Microwave methods are employed due to the dramatic decrease in the synthesis time, which can be explained by the faster and more uniform heating rates, rapid dissolution of precursors, and creation of hot spots.

In sono-chemical intensive ultrasonic radiations (20 kHz–10 MHz). It is applied to the reagents resulting in chemical changes[29].

Mechano-chemical work by the agitation and collision between reagents. It provides access to more green chemistry approaches since it is a solvent-free method. Electrochemical synthesis, mainly done by the method of anodic dissolution, uses an electrode as a source of metal ions, so no metal salts are required. This method offers a continuous production of MOFs.

The methods are summarized in Figure 2.6[30]

Figure 2.6: Synthesis Methods

2.5 Zirconium MOFs

In general, MOFs exhibit relatively low chemical and mechanical stability. However, the use of Zirconium as a central metal, with high charge density Zr^{4+}, and knowns as a strong Lewis acid with a high affinity for oxygen and carboxylate-based ligands resulted in a solid Zr-O bond and Zr-(COOH) that tether the organic and inorganic moieties. So, Zr-MOF possesses exceptional thermal and chemical stabilities. In addition, they have shown large specific areas and structural and chemical tenability. This outstanding performance is also attributed to the defective open acidic positions (uncoordinated Zirconium sites). These extensive features also endow them as promising materials for heterogeneous catalysts. This includes the previously

known types of catalytic reaction over Zr-MOFs, and their functionalized derivatives, including Lewis acid catalysis, Bronsted acid catalysis, oxidation catalysis, biomimetic catalysis, electrocatalysis, and photocatalysis[31].

Chapter 3 Characterization Techniques

3.1 X-Ray Diffraction

It is a technique that is used for the investigation of the crystallographic structure and fine structure of matter. It was discovered by Laue's in 1912 that electromagnetic waves between 200eV and 1Mev reveal the structure of the crystal. The sample is irradiated by X-Rays and the intensity and the scattering angles are measured in return. This range of wavelengths has the same order of magnitude as the crystal dimensions of the material, so it is possible for diffraction phenomena to occur.

When the X-Ray encounters the sample, coherent radiations are diffused spherically in all directions, where these radiations diffused from different crystal planes interfere together. At certain angles constructive interference will take place whereas on other angles destructive ones, where only constructive interferences will appear on the diffractogram[32]. The following figure demonstrates Bragg's conditions to have constructive interference. The waves diffused from different reticular planes must be in phase after the other waves have accounted for the extra distance by an integer multiple of the wavelength. That leads to AB + CD = nλ. Furthermore, the trigonometry gives AB + CB = 2dsinθ. Bragg's law calculates the angle where constructive interference from X-rays scattered by parallel planes of atoms will produce a diffraction peak. The diffraction phenomenon is shown in Figure 3.1[33]

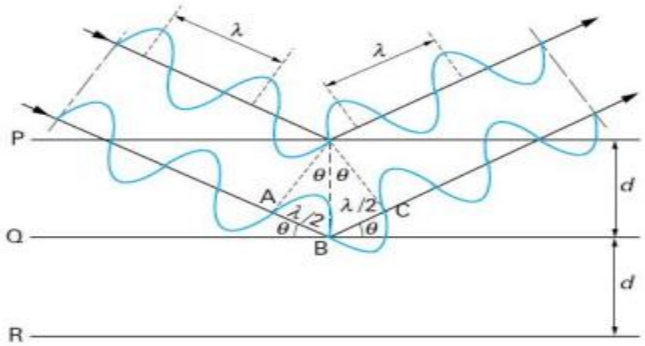

Figure 3.1: XRD phenomenon

3.1.1 Scherrer equation

It is the most common equation used to approximate the crystalline size is given by equation 3.1.

$$L = \frac{K\lambda}{B\cos\theta}$$

Equation 3.1: Scherrer equation

L: Nanocrystal size

K: Shape factor

λ: Wavelength of radiation in nanometer ($\lambda_{CuK\alpha}$ = 0.15405 nm)

θ: Diffracted angle of the peak

β: Full width at half maximum of the peak in radians related to the broadening of the peaks[34]

Broadening in the peaks is related to physical broadening and instrumental broadening. To account only for the sample contribution and eliminate the instrumental contribution, equation 3.2 is applied.

$$\beta^2_d = \beta^2_m - \beta^2_i$$

Equation 3.2: Gaussian equation describing the relation between total error and instrumental error

β_m: Measured broadening,

β_i: Instrumental broadening, which is a combined effect of photon source energy, spatial and angular divergence distributions of the photon beam, modeled by the specific optical setup and the quality of its elements, and radiation–matter interaction[35].

β_d: Corrected broadening responsible for the crystal size.

3.1.2 Lattice constant

The lattice parameter of the fluorite phase has been calculated by unit cell refinement using the software Unit-Cell.

For cubic geometry, the inter-planar space is given by equation 3.3

$$d_{hkl} = \frac{a}{\sqrt{h^2+k^2+l^2}}$$

Equation 3.3: Interplanar distance in cubic geometry

substituting equation 3.3 in equation 3.1

$$a = \frac{\lambda\sqrt{h^2 + k^2 + l^2}}{2\sin(\vartheta)}$$

Equation 3.4: Lattice constant in cubic geometry

For each sample, a set of lattice constants are calculated from the main peaks reported before, and then the arithmetic average is reported.

3.1.3 Diffractometer

A diffractometer is made of an x-ray tube, a goniometer, a detector, and slots to control the beam. As the sample is immobile, the tube turns at an angle of θ/min, and the detector also. This method applies to θ:θ instruments such as PANalytical, which was used for our characterization. The X-ray intensity is usually recorded as "counts" or as "counts per second. The apparatus is shown in Figure 3.2[36].

The correct assessment of the diffractogram is verified either from JCPDS files that are specific for each sample. For our synthesized MOF, no available database was found. So the correct assessment was done by comparing the experimental XRD with reference ones that are usually simulated. In such cases, an exact and complete match between the experimental and reference patterns is needed. Arbitrary peaks predicted by a reference pattern cannot be missing in the experimental XRD data without justification[37].

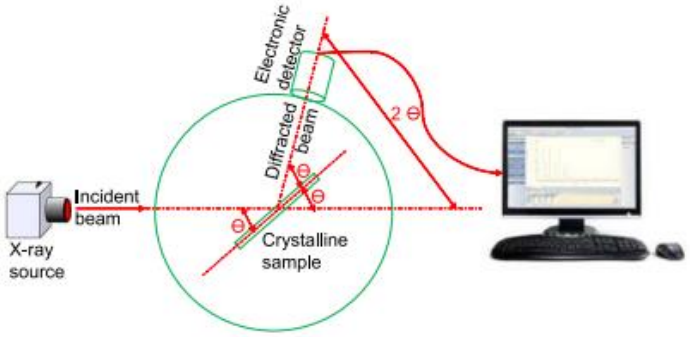

Figure 3.2: XRD Apparatus

3.2 Brunauer-Emmett-Teller Analysis

When nitrogen is in contact with a solid at 77K, the molecules will be attracted to the surface by Van der Waals week forces. This process is called physisorption where it is thermodynamically reversible at isothermal conditions, which is not in the case of chemisorption. The volume of the adsorbed nitrogrn depends on the relative pressure and the solid surface[38].

As pressure increases, the condensed N_2 starts by filling small pores and increasingly large surfaces nano-pores. They are divided into micro- (diameter ≤ 2 nm), meso- (diameter ≤ 50 nm), and macro-pores (diameter ≥ 50 nm)

Brunauer-Emmett-Teller (BET) theory is still the most widely used procedure for explaining the physical absorption of gas molecules on solid surfaces at cryogenic temperatures that results in assessing the textural properties of nano-materials by approximating surface area, pore-volume, microporous area, etc.[39]. The mechanism of adsorption is represented in

Figure 3.3[40] It is an extension of Langmuir's theory, which considers that multi-layers of adsorbed molecules are formed. The theory consists of 4 assumptions:

1. Langmuir equation can be applied to every single layer of adsorption

2. Adsorption and desorption occur only in exposed areas.

3. Equilibrium between the adsorption of the i^{th} layer and the desorption of the i+1 layer

4. the molar heat of adsorption is higher for the first layer and is equal to the heat of liquefaction of vapor for the latter

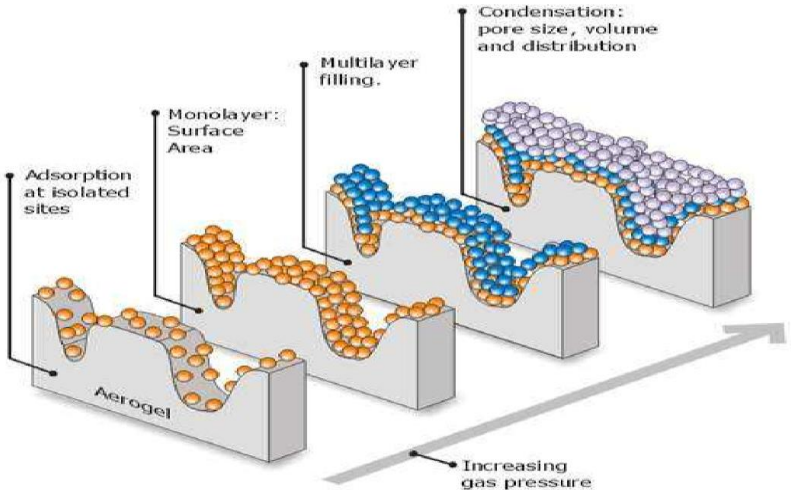

Figure 3.3 Adsorption process following BET theory

$$\frac{Q}{Q_m} = \frac{Cx}{(1+x)[(1+(C-1)x]}$$

Q: Amount of vapor adsorbed

x: P/P_0 with P the equilibrium pressure

C: Constant related to the difference between heat for adsorption in the first layer and heat for liquefaction of the vapor

Q_m: Monolayer capacity of the adsorbed vapor on the solid.

$$\frac{x}{Q(1-x)} = \frac{(C-1)x}{cQ_m} + \frac{1}{CQ_m}$$

C and Q_m could be obtained by plotting $x/[Q(1-x)]$ versus x. This plot yield a line in the interval $0.05 < x < 0.30$. For higher values, this model is no more valid.

$$a_s = \frac{Q_m . L . \sigma_m}{m}$$

L: Avogadro constant

σ_m: Molecular cross-sectional area and m the mass of the sample

At high pressure, the pores will be filled by molecules which are referred to as pore condensation where gas condensates to a liquid-like phase. At this stage, BJH analyses are used to approximate pore volume and size distribution.

Despite the weakness of its theoretical background, the BET area is considered to estimate the surface area of microporous and mesoporous materials known to be as the probe-accessible area, which is the effective available area for desorption of a specific adsorbate. BET by theory can be applied only to type and IV isotherms, where extreme caution has to be considered when applying it in the microporous range (type I). Where is impossible to separate the process of monolayer-multilayer adsorption where BET can be applied (linear range) from micro-pores filling[41].

Adsorption isotherm expresses the relation between the adsorbed volume of nitrogen and the equilibrium pressure at isothermal conditions. However, desorption isotherm is obtained by decreasing the pressure. The volume adsorbed depends on the mass of the solid, temperature, and the equilibrium pressure reached. For a given solid, at a fixed temperature, the adsorbed mass is only depending on P[42]. Based on the shape of the isotherm and the difference between the adsorption and desorption isotherm, six main types of isotherms are identified (Type I to VI), and five hysteresis loops are identified: H1to-H5.

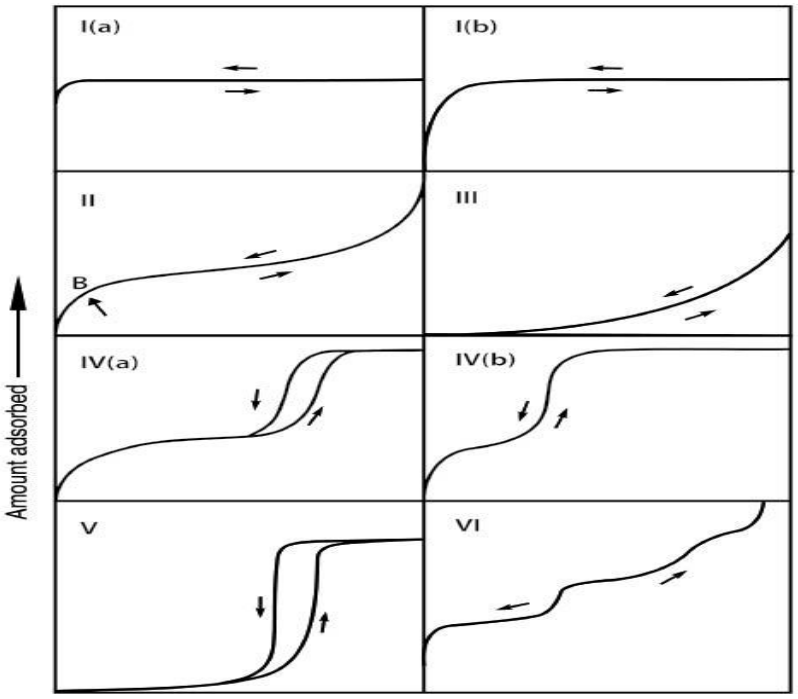

Figure 3.4: N_2 Adsorption isotherms classification

Type I isotherms is a characteristic of microporous solids with relatively small external surfaces.

Type II is a characteristic of nonporous or macroporous materials.

Type III isotherm is a characteristic of weak interaction between material and adsorbed gas; no identified monolayer formation.

Type IV isotherms are a characteristic of mesoporous solids.

Type V isotherms are a characteristic of water adsorption on hydrophobic micro-meso porous structures.

Type VI is a characteristic of highly uniform nonporous structures.

Hysteresis loops

Type H1 loop is characteristic of material possessing a narrow range of uniform mesopores.

Type H2 is characteristic of a more complex pore structure which can be attributed to pore blocking or evaporation caused by cavitation.

Type H3 characteristic of non-rigid aggregates.

Type H4 is a characteristic of zeolite crystals and micro-meso porous activated carbons.

Type H5 is a characteristic of structures having both open and partially blocked pores.[43]

3.3 Thermo-gravimetric Analysis

Thermo-gravimetric Analysis (TGA) is classified as a type of thermal analysis that quantitatively measures the relative changes in the mass of the material as a function of time or a controlled temperature program[44]. This technique is useful in determining the thermal stability of the MOF and to estimate its solvent-accessible pore volume[45].

TGA is equipped with a precise analytical quartz crystal microbalance that is placed inside the combustion furnace. The combustion is held under a constant flow of gas to remove gaseous decomposed products and prevent condensation of water vapors on the walls of the instrument. The mass fluctuations of loss or gain are the result of physical reactions taking place. For instance, drying can be directly seen as a quick initial drop at the beginning of heating. Other physical reactions can include Adsorption, Desorption, Crystallization, Melting, Vaporization, and sublimation. Regarding chemical reactions, reduction, decomposition, oxidation, and dehydration, the chemisorption can induce mass change[46].

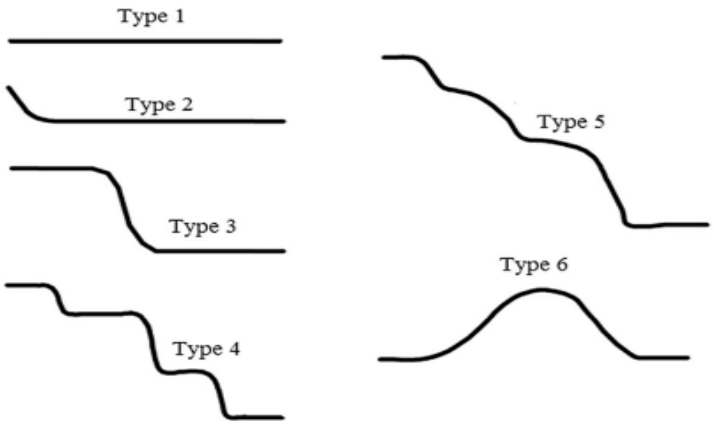

Figure 3.5: TGA classification curves

The different profiles of weight losses are reported in Figure 3.5[44]

Type1: No weight variation over the whole covered range, can be related to thermal stability.

Type 2: Initial mass drop followed by the constant line, mostly related to drying of volatile compounds.

Type 3: Single-stage weight loss.

Type 4: Multiple stages of weight loss.

Type 5: surface oxidation reactions.

Type 6: Product decomposes at a higher temperature.

3.4 ^{1}H NMR Spectroscopy

Nuclear magnetic resonance, NMR, is a technique that studies atomic nuclei based on their property, the quantum number of nuclear spin I. When a nucleus with I ¹ 0 is subjected to an external magnetic field, the degeneration of energy levels is lost. associated with it, due to the interaction of the applied magnetic field with the magnetic moment of the core. The energy difference between the energy levels determines a population difference (according to a Boltzman distribution) and it is precisely the latter that allows us to observe the nuclear spin transition and therefore the NMR signal. The main application of NMR spectroscopy arises from the observation that the transition frequency of an atomic nucleus measured by the spectrum is closely related to its chemical neighborhood of the nucleus. Unlike the spectra obtained from liquid samples, those relating to solid systems suffer from a low resolution, in fact they show very large peaks. The absence of high resolution is due to the interactions to which a nuclear spin is subjected. These interactions depend on the orientation, fixed in solids, of the nuclear spins with respect to the magnetic field. Absorption for all possible orientations of the nuclei with respect to the magnetic field is observed simultaneously, resulting in very large peaks.[47].

The individual peaks of an NMR spectrum are mainly characterized by three parameters: the "chemical shift" (position of the peak), the intensity (integrated area of the peak) and "linewidth" (width of the peak at half height). These parameters are closely related to the chemical structure of the analyzed sample, hence their use in structural studies. In addition, other parameters such as relaxation time and spin-spin coupling constant can give specific information[48] An illustration of the NMR phenomenon is shown in Figure 3.6[49]

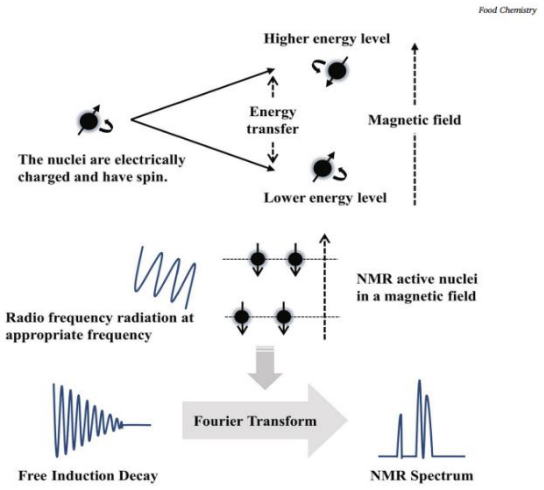

Figure 3.6: NMR spectroscopy illustration

3.5 Scanning Electron Microscopy

Scanning electron microscopy is based on bombarding the sample with high-energy electron beams where these interactions will reveal information about the sample including its texture, chemical composition, and crystallinity. The electron beam pass through a series of lenses and apertures that act on focusing it[52]. This whole process occurs under vacuum conditions to prevent any atom or molecules from interacting with the electron beam. The data is collected over a selected surface area, and a 2-D image will be generated that displays spatial variations in these properties[53].

Chapter 4 Scope of the work

Methyl Levulinate is an integral derivative of Levulinic acid that can be used to synthesize many valuable chemicals. Several synthesis methods have been studied in the literature.

The most classic traditional method for synthesizing Alkyl Levulinates is done by esterifying LA using different acid catalysts and alcohols as reagents. The reaction scheme is shown in Figure 4.1[54]

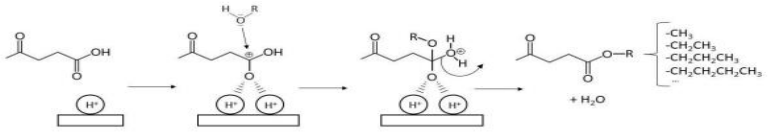

Figure 4.1: Esterification reaction illustration on solid catalyst

Using bio-feedstocks provides a cheap and sustainable alternative route for the production of Alkyl Levulinates. However, due to the variable composition and unknown sugar content, the reaction generates multiple intermediate products and results in a low yield reaction as shown in Figure 4.2[2]. In the case of Lignocellulosic materials, the recalcitrance and insolubility of the reactants in the reaction medium added to the necessary steps of de-polymerization, solvolysis, and thus dehydration, making the overall process require drastic conditions. Monosaccharides given by C5/C6 sugars such as xylose, fructose, and glucose formed from disaccharides and polysaccharides are also used as precursor molecules for the synthesis of Alkyl Levulinates. Same challenges are suffered in these reaction routes from the insolubility of the reactants in alcohols and the multi-intermediate products. In addition, such a reaction requires a high temperature of treatment for catalyst activation, increasing energy consumption and imposing additional costs regardless of the cheapness of the used feed-stocks (Table 4.1).[55]

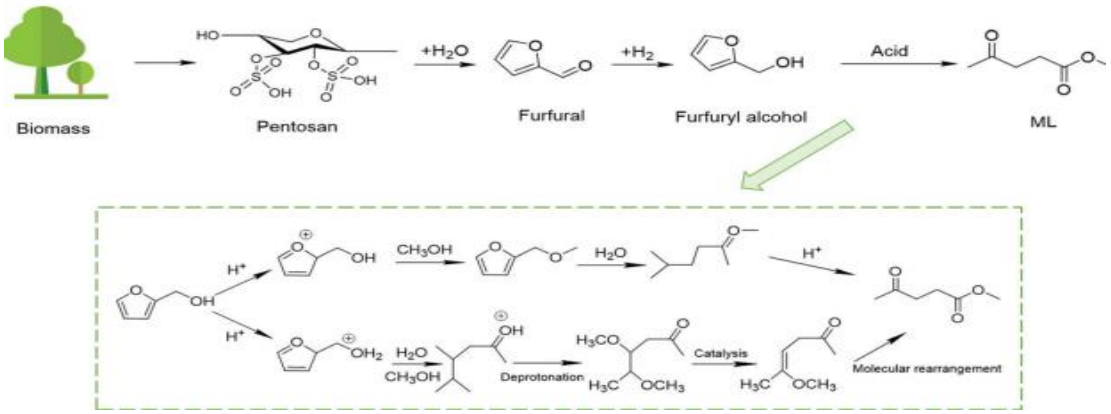

Figure 4.2: Reaction pathway of ML from biomass

Table 4.1: Overview of reaction conditions for the conversion of biomass to ML using classical acid catalysts

Raw material	catalyst	Temp(°C)	Reaction time(hr)	Yield(%)	ref
Cellulose	Methanol	200	1.5	34.1	[56]
	Nbp-pH$_2$	180	24	56	[57]
glucose	Solid acid al MCM	220	6	38	[58]
	SO_4^{2-}/TiO_2	200	2	35.0	[59]

Research progress

However, in this thesis we are proposing a new synthesis route, still under preliminary investigation in the scientific literature, starting from Ethyl Levulinate. The choice of LA derivatives to conduct such reactions is of high interest due to the moderate reactivity of the carboxylate group that can increase the selectivity toward the final products[60]. In addition to their low boiling point, they allow easier and cheaper separation.

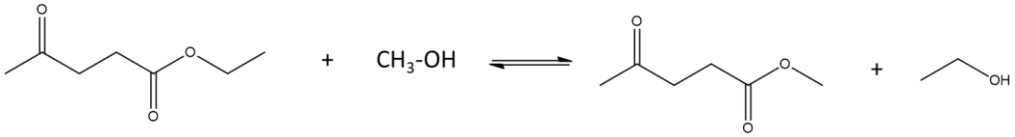

Figure 4.3: ML synthesis reaction from EL

Regarding catalyst support, transesterification reactions are promoted by acid catalysts, mostly activated at high temperatures and show low stability to leaching. Stable catalysts in transesterification were not found yet, opening a route to the development and optimization of a new class of materials, that can also be activated at a lower temperature.

4.1 MOF-808

MOF-808 serves as a potential candidate to drive such reaction effectively endowed by its high chemical tunability due to its ordered crystalline typology and low connectivity of the Zirconium cluster that can provide more accessible sites for catalytic reactions. Is it also shown that MOF-808 can possess the highest surface area among other MOFs which can be a remarkable advantage for selecting it for further catalytic applications. The metal SBU unit is given by $Zr_6O_4(OH)_4(HCOO)_6(CO2)_6$, noted by Zr_6 for simplification. Each Zr_6 node cluster coordinates with six BTC linkers where each of these linkers is connected to 3 metal clusters. The synthesis of MOF-808 is reported to give octahedral crystals with general formula represented as $Zr_6O_4(OH)_4(BTC)_2(HCOO)_6$.. Tetrahedral cages with internal pore diameters of 4.8 Å are formed, with the inorganic SBUs at the vertices and the BTC linkers at the faces of the tetrahedron[61]. A large adamantane cage is formed with an internal pore diameter of 18.4

Å. Single crystal diffraction data analysis shows that MOF-808 crystallizes in the cubic space group $Fd\bar{3}m$ with lattice parameter a = 35.076. The large adamantane-shaped cages (⌀ ~ 18.0 Å) are accessible by its hexagonal windows (⌀ ~ 10.0 Å)[62] . All these features are reported in Figure 4.4.

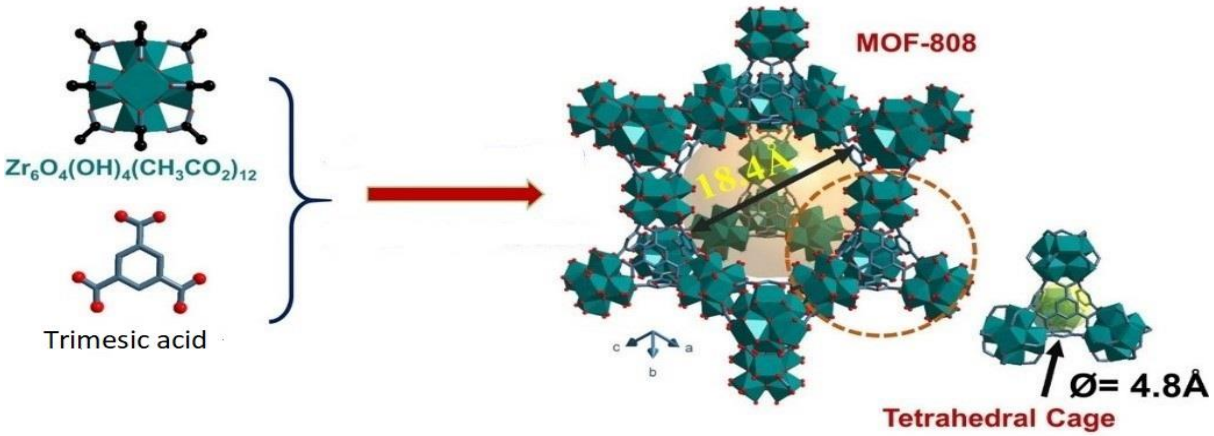

Figure 4.4: Schematic representation of MOF-808 modified from [76]

There is still no standardized procedure to be followed that results in the best MOF-808 characteristics needed to drive such reaction effectively whether from the surface area, crystallinity, stability, or presence of active sites. Also produced MOFs are usually lacking uniformity, crystallinity, and porosity as they are obtained without size control methods. Thus, the establishment of high-quality MOFs with tunable porosity and reactivity can open some new perspectives for catalyst studies.

Although the literature study is intensive regarding MOF, a systematic analysis of the synthesis process itself and of the effect of the different variables that intervene in it are rather scarce. Therefore, the objective of this paper is to rigorously assess the intrinsic effect of the use of different synthetic approaches and assess the direct effect of varying parameters on the chemical and physical properties of the synthesized MOF, followed by a study of these different characteristics on the yield of the reaction.

These parameters can include general procedure steps, such as the washing reagents used, magnetic stirrer RPM, and mode of addition of reagents. Other more specific parameters can include temperature and time of the synthesis, activation temperature, molar ratio, concentration, precursors used, etc.

4.2 Characteristics to be studied

4.2.1 Crystallinity

The structural uniformity of the active sites within the framework allows fundamental investigation of the structural and catalytic properties of the studied MOF, in contrast to

siliceous mesoporous materials with amorphous walls. MOF crystallinity is the first route for obtaining materials of tunable morphology and composition[63].

4.2.2 Surface Area

In heterogeneous reactions, the collision between reactants occur at surface interface between the two reagents. Hence, the number of collisions per unit time depends on the available surface area that can increase the chances of effective collision[64]. Active sites that are usually formed on the material surface will increase in number as the porosity and surface area increase, leading usually to greater catalytic activity.

4.2.3 Defects

The substitution of organic ligands by modulator agents during the synthesis will allows the better modulation and engineering of the MOF-808 structure to enhance the structural accessibility of zirconium centers by other reagents without framework collapse[65]. Introducing more defects into the framework will lead to the formation of open zirconium metallic sites with Lewis acidity. Both defects and acid metal sites will boost the catalytic activity of the catalyst by providing more diffusion paths and active sites respectively.

Chapter 5 Experimental Work

In literature studies, MOF-808 has been designed following different procedures and parameters with a non-unique or reliable synthesis approach that can allow the development of a well-ordered material [66] [67]. In other words, it's still absent a rational synthetic design for MOF-808 that can result in recognized chemical and physical properties that allow the material to be used in further applications.

The present research work concerns with the synthesis and characterization of Zirconium MOF-808 catalyst followed by testing the catalyst in a novel procedure to obtain methyl levulinate from ethyl levulinate. Analysing the most promising synthesis procedures reported in the literature, we start our first synthesis by exploiting a solvothermal approach using formic acid as a modulator, $ZrOCl_2.8H_2O$ as a precursor and N,N Dimethylformamide (DMF) as one of the most common solvent used for MOF's synthesis, all dissolved in a reaction system with a $ZrOCl_2.8H_2O$/BTC molar ratio=1:1 and synthesized for 72 hours.

After the characterization of this sample, the reaction protocol is then changed investigating the effect of the most important synthesis parameters. Different synthesis approaches lead to the formation of the different samples, as well described in the following parts.

The first parameter that was investigated is the synthesis time exploiting other two different durations at 24 and 48 hours. Then the role of the amount of acidic modulator was assessed by decreasing the volume of formic acid. The next parameter investigated is represented by the use of an alternative precursor to oxychloride, which is zirconium tetra-Chloride ($ZrCl_4$). The same followed synthesis protocol using formic acid was carried out at a molar ratio of Zr/BTC=3:1 followed by a change in synthesis time. Finally, we investigated the role of the acidic modulator by using acetic acid instead of formic acid.

To eliminate the effect of temperature on MOF typology, the synthetic temperature was held fixed at 110 °C.

5.1 Synthesis Protocol

The different chemicals used during the synthesis are given in Table 5.1.

Table 5.1: Chemicals used during synthesis

Product	CAS	Manufacturer
DMF	68-12-2	Sigma-Aldrich,99.8%
$ZrOCl_2.8H_2O$	13520-92-8	Alfa Aesar,99.9%
$ZrCl_4$	10026-11-6	Sigma-Aldrich, >99.9%
BTC	554-95-0	Sigma Aldrich,95%
Formic Acid	64-18-6	Sigma Aldrich, >95%

Acetic Acid	64-19-7	Sigma-Aldrich >99.8%
Methanol	67-56-1	Merck KGaA

Synthesis Procedure

$ZrOCl_2 \cdot 8H_2O$ was dissolved in a mixture of DMF (20ml) and the acidic modulator (37ml of formic acid, AF), and left stirred for 20 minutes. Trimesic acid was dissolved in 20 mL of DMF by sonication and added dropwise to the initial solution. The mixture was stirred for an additional 10 min. Subsequently, the mixture was sealed in a Teflon bottle and heated to 110°C for a fixed period of time (24, 48 or 72 hours).

Washing step

After the Teflon bottle is cooled down at room temperature, 20ml of DMF is added to the bottle to dissolve unreacted precursors. The solution is then centrifuged at (10000RPM,17°C,10min). Second step centrifugation is done with the same conditions after the liquid phase is wasted and another 10ml of DMF is added. The deposited solids are washed with acetone and methanol and then filtered using a vacuum system.

Drying step

The collected crystals are collected into a watch glass and then put into the oven to dry at 100°C for 4 hrs. The crystals are then ground and put in the oven again for 2hrs at 80°C.
The obtained samples are named Zr-MOF *MODULATOR - MOLAR RATIO Zr/BTC - TIME.*

5.2 Characterization

N_2 Adsorption Measurements

The textural properties are determined by nitrogen adsorption at 77 K, using an ASAP 2020 Instrument. The sample is deposited in a 9 mm cell burette closed by a rod to reduce the void space and then the mass of the sample was determined precisely in the range of 50-80 mg. The burette is mounted on the degas station of the system for a duration of 12h at 110°C to remove any guest contaminants. After this operation, the samples could have lost weight which requires a new weight measurement before starting the adsorption measurement. A dewar of liquid nitrogen is used to maintain a low constant temperature and ensure a strong enough adsorption of nitrogen molecules on samples surface.

The measurements methods adopted to evaluate the textural properties of materials are reported here:

1. Total pore volume was calculated using single point adsorption at a relative pressure approximately tending to unity.

2. Microporous volume and area are calculated from the t-plot. It is a method that allows the determining of microporous area and volume by plotting the volume of adsorbed nitrogen with respect to the statistical thickness of an adsorbed layer on a reference non-porous

support[68]. In our case, the reference curve used for comparison was Harkins-Jura, with a pressure range corresponding to the short and large diameter thickness of the Nitrogen atom is between 0.3 and 0.4nm

3. Pore size distribution is obtained by applying the density functional theory (DFT) between 10Å and 50Å. DFT is a procedure based on fundamental statistical mechanic theories that are applied to describe the molecular behavior of fluids in porous media. In our case, the pores are assumed to have a cylindrical typology endowed by the literature modeling of MOF-808, and the model of oxide surfaces was used to describe the process of N_2 adsorption.

4. Langmuir surface area was calculated directly from the obtained Langmuir plot in the range between 8 and 20kPa. It provides means of determining the surface area based on a monolayer coverage of the solid surface.

X-Ray Diffraction

X-ray powder diffraction (XRPD) patterns were obtained on an X'Pert Phillips diffractometer operating with Cu Kα radiation (1.541874 Å) and equipped with a PIXcel 1D detector (step: 0.026°2θ; time per step: 2 s) where 2θ ranged from 2° to 50°.

Thermo-Gravimetric Analysis

The thermal stability of the synthesized materials was evaluated by Thermo-gravimetric analysis (TGA). TGA was performed on a LINSEIS STA PT 1600 apparatus using a heating rate of 5°C min^{-1} under Argon flow of 60sccm/min and raising the temperature to 800 °C.

Scanning Electron Microscopy

Powder samples were deposited onto conductive carbon tabs mounted on an aluminium stub and coated with Au-Pd. The prepared samples were transferred to and imaged using NOVA NANO FEG-SEM450 electron microscope, operating at an acceleration voltage of 5 kV.

5.3 The role of Synthesis parameters

5.3.1 Effect of Synthesis Time

In most studies handled before regarding MOF-808, the synthesis was carried out for a long time reaching 7 days. However, in this study, the maximum synthesis time used was 72 hours resulting in almost the same characteristics and properties of those reported in literature. Table 5.2 reports the conditions applied for the synthesis of the different samples.

Table 5.2: Samples synthesized with molar ratio 1:1 under different synthesis time

Sample code	Molar ratio (Zr/BTC)	$ZrOCl_2.8H_2O$ (M)	BTC (M)	Acid volume(ml)	Temp (°C)	Time (h)
Zr-MOFAF 1:1,72hr	1:1	0.0468	0.0468	37	110	72
Zr-MOFAF 1:1,48hr	1:1	0.0468	0.0468	37	110	48

Zr-MOFAF 1:1,24hr	1:1	0.0468	0.0468	37	110	24

XRD characterization was performed to monitor the extent of crystallization and evaluate the crystal size.

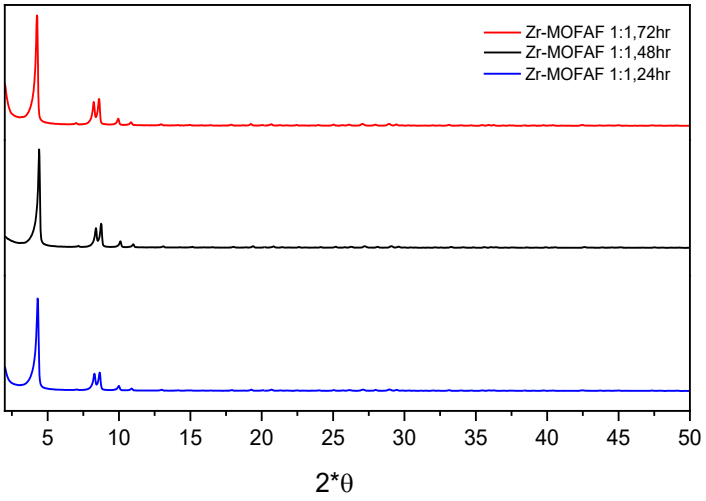

Figure 5.1: Diffractograms of Samples synthesized with molar ratio 1:1 under different synthesis time

In Figure 5.1, all samples possess the main peaks at 4.2°, 8.24°, 8.66°, 9.98°, and 10.9° corresponding to Miller indices of (111), (311), (222), (400), and (331) as reported by Zhou et. al[69] for the MOF-808.

All the samples show relatively same intensities irrespective of the synthesis time followed, which indicates the effectiveness of the synthesis of the MOF-808 crystalline phase. However, it's not possible to distinguish any crystallinity differences between the samples unless treating the diffractograms to extract cell data, obtained with Unitcell software. We can recognize a relative change in the crystallinity size and cell parameters as reported as shown in Table 5.3.

Table 5.3:XRD Data obtained from Diffractograms ·

Sample code	Cell parameter(Å)	Cell volume(Å^3)	Crystallite size (Å)
Zr-MOFAF 1:1,72hr	35.59983	45117.37	1425
Zr-MOFAF 1:1,48hr	35.08281	43180.05	1828
Zr-MOFAF 1:1,24hr	35.46972	44624.59	1216

Analyzing the reported data, MOF-808 crystallinity gets enhanced with increasing reaction time from 24 to 48 hours, but a further increase in reaction time up to 72 hours results in a

decreased crystallinity, which allow us to hypothesize that too long reaction time causes a sort of reorganization in the structure. The same trend was found in the textural properties. This can be also seen when the sample treated for 72hours shows the lowest micro-pore peak intensity at 18 Å and the highest mesoporous distribution.

The morphology of the samples is further assessed using SEM. The results are reported in Figure 5.2.

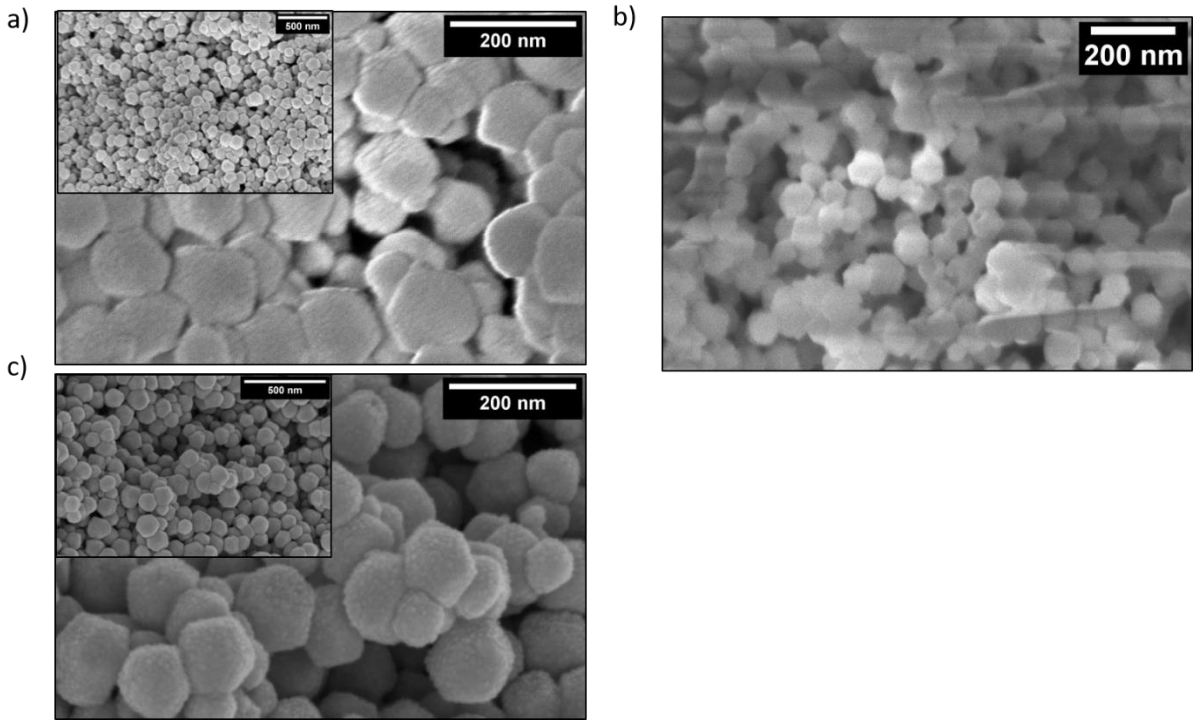

Figure 5.2: SEM Micrographs of MOF samples with formic acid as modulator and molar ratio Zr: BTC 1:1 synthetized for 72h a), 48h b) and 24h c). In the inserts are reported the wide view at low magnification.

At high magnification, a visible difference into the shape of obtained materials is observed. The 72 hours sample shows a non-homogeneous hexagonal nanoparticles which is more flat compared to the other two samples. In particular, the 24 hours samples shows a typical tetragonal shape of MOF-808 particles. These results seem to support the previously hypothesis regarding a structure reorganization with higher reaction time.

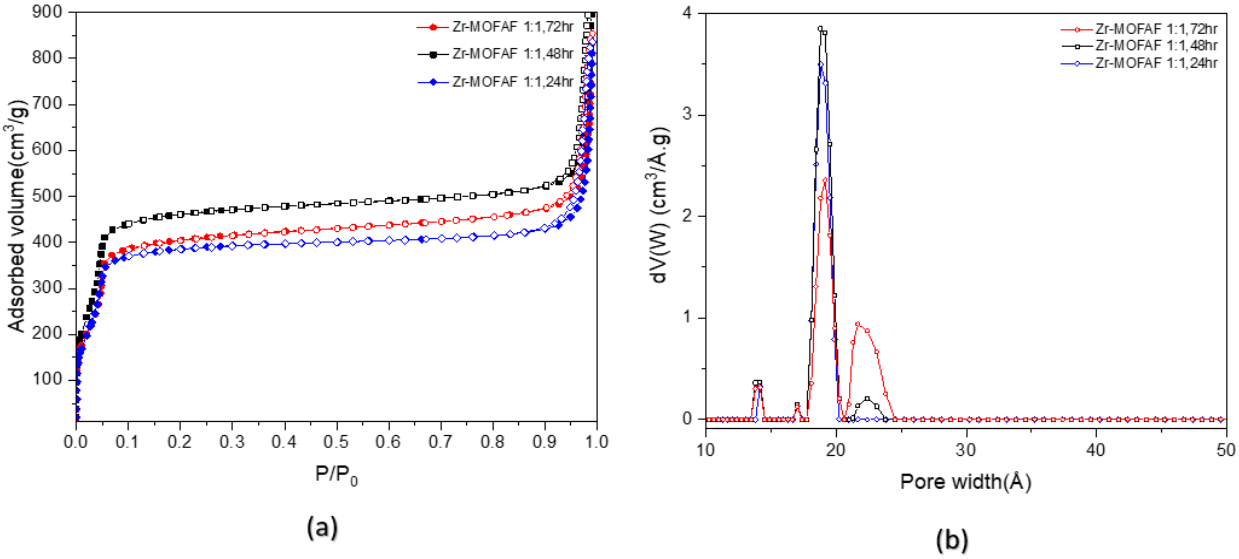

Figure 5.3: Formic acid samples synthesized with molar ratio 1:1 with different synthesis time (a)N_2 Adsorption-Desorption isotherms (b)Pore size distribution

Table 5.4: Data obtained from N_2 isotherms

Sample code	BET(m^2/g)	Total pore volume(cm^3/g)	Microporous area(m^2/g)	Microporous volume(cm^3/g)	Langmuir Area (m^2/g)
Zr-MOFAF 1:1,72hr	1619	1.321	897.395	0.367984	1977
Zr-MOFAF 1:1,48hr	1764	1.633	1026.5456	0.409464	2103
Zr-MOFAF 1:1,24hr	1475	1.294	906.7990	0.362271	1747

The N_2 adsorption isotherms shown in Figure 5.3(a) exhibit the characteristics of isotherms as a combination between type I and type IV isotherms formulating the presence of microporous and mesoporous textures. The sudden increase in the adsorbed volume accompanied by a very mild hysteresis for a relative pressure greater than 0.9 can be caused by mesoporous filling and adsorption in the inter particles [70]. The values of specific surface area, total pore volume, microporous and volume were obtained by the elaboration of the isotherms are reported in Table 5.4.

The identical trend in the N_2 adsorption-desorption isotherms and the associated hysteresis shown between all the samples can indicate the similarity in the connectivity and typology of the pores.

The sample synthesized with 48 hours shows the highest nitrogen uptake, followed by the sample treated with 72 hours, and then the sample synthesized with a duration of 24 hours. This order is also consistent with the reported values of BET and Langmuir areas in Table 5.4

According to Figure 5.3(b), All the samples possess the microporous main peak at an average of 18.4Å which is a characteristic of the MOF-808. The pore sizes at 4.8Å and 10Å could not be investigated by this method. These peaks are consistent with the MOF architecture as reported in the literature. In addition, all the samples possess two other peaks exhibited at 14Å and 17Å related to microporous textures that can indicate the presence of material with more ordered and developed pores. Another distribution is shown around 22Å the 72h and 48h samples, which is related to the presence of mesoporous textures. The samples with the highest reaction time show a higher presence of mesopores, that decrease decreasing the time until to not be more detected with the sample 24h.

In addition, the sample treated for 48hours shows the highest microporous peak intensity at 18 Å followed by the sample treated for 24 hours and then by the sample treated for 72hours. This order in peak intensities follows the same order as the reported microporous area Table 5.4. As a general trend, the order shown in crystallite size was followed also in the reported BET and Langmuir areas.

The thermal stability of the samples is characterized by TGA analysis which allows further determination of other characteristics such as defects. The obtained curves are presented in Figure 5.4.

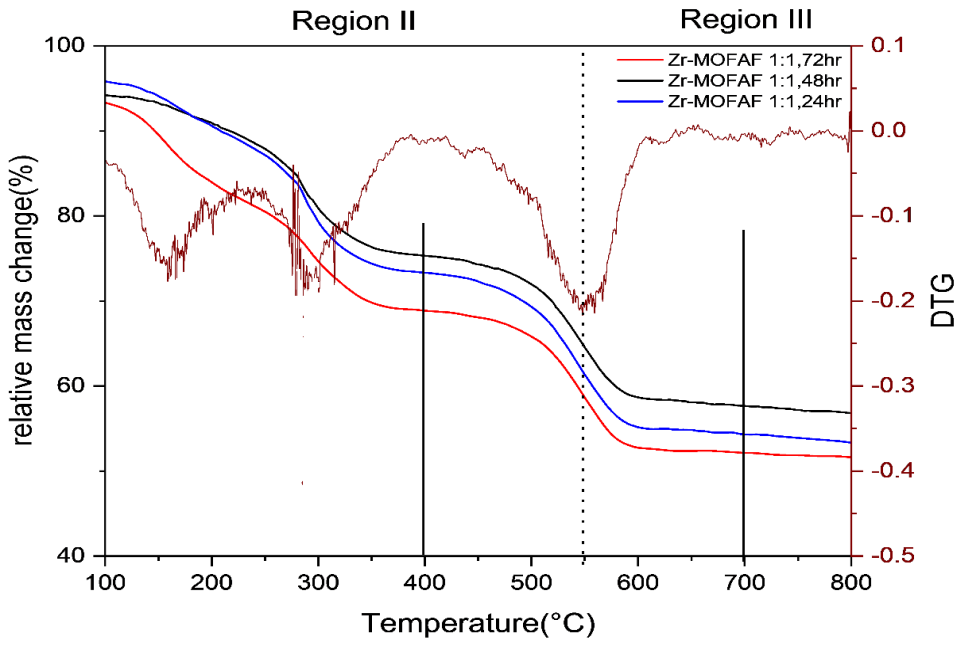

Figure 5.4: Thermo-grams and DTG plots of Formic acid samples synthesized with molar ratio 1:1 with different synthesis times. The dotted line is used to separate different regions. Solid lines are used to calculate defects.

Table 5.5: Data obtained from Thermo-grams

Sample code	Total weight loss(%)	Solvent weight loss(%)	Organic weight loss(%)
Zr-MOFAF 1:1,72hr	48.36	6.69	27.51
Zr-MOFAF 1:1,48hr	43.18	5.80	22.24
Zr-MOFAF 1:1,24hr	46.67	4.2	26.49

In region I, the weight loss is related to the evaporation of adsorbed water varying from room temperature up to 100°C, while in region II the mass loss is related to the removal of modulators, linkers, solvents, and dihydroxylation of zirconium clusters varying from 100°C up to 550°C. The weight loss in region III is related to the total collapse of the structure and thermal decomposition into zirconium oxide varying from 550°C up to 800°C according to the below reaction[71].

$$Zr_6O_4(BTC)_{2(s)} + \text{heat} \rightarrow 6ZrO_{2(s)} + \text{gaseous products}$$

The decomposition of the organic ligand is observed for all the samples roughly at 540°C. It can be deduced that the framework of all the samples has similar thermal stabilities, and the surface chemistry wasn't modified despite the change in crystallinity and the differences detected before [72].

This can also be proved by the identical DTG plots of all the samples, showing the main peaks at the same temperature. For that reason and clearer figure, only one DTG plot was reported that matches the DTG plots for all the other samples. In addition, all the thermograms show a kind of plateau between 400°C and 500°C indicating thermal stability in this range.

Theoretical Defects Calculation

The exact number of defects wasn't calculated since the total loss at 800 °C is about 44 wt %(Table 5.5) which is higher than the theoretically normalized value which is 38.5 wt%[73].This can be related to the presence of water and Formic acid that can be still coordinated with the SBUs. In addition, the TGA analysis was done using Argon gas which may not guarantee the complete oxidation of the sample. But as a rule of thumb, defects are inversely proportional to the mass loss between 400°C and 700°C[74]. For the calculation of a qualitative approximation of the concentration defects, the following equation was used:

$$defects = \frac{1}{\%m(700°C) - \%m(400°C)}$$

The difference in weight loss in region 1 can be due to the capacity of retaining adsorbed water which is a direct consequence of the modification of porous structure and surface area[72].

Different total weight loss can be attributed to the different adsorbed solvents within the pores[75].

Results Summary

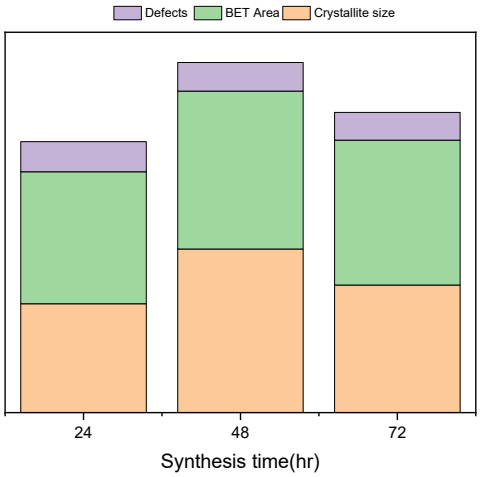

Figure 5.5: Results summary of Formic acid samples synthesized with molar ratio 1:1 with different synthesis time

In the above bar graph represented in Figure 5.5, we can easily recognize that the maximum crystallinity and surface area are attributed to the sample synthesized within 48 hours of treatment. Defects concentration is almost the same for the samples with different synthesis times. In general, all the samples seem of interest for further catalytic applications.

5.3.2 Effect of Formic acid volume

The role of the acidic modulator in the synthesis of MOF-808 is to be assessed by synthesizing a new sample, through the same procedure used before reported in section 5.1 Synthesis Protocol, but reducing by half the content of formic acid (18,5ml). The resulting sample is named Zr-MOF$_{50\%}$. The sample Zr-MOFAF 1:1,24hr, previously described, has been used as reference material to evaluate the properties of Zr-MOF$_{50\%}$.

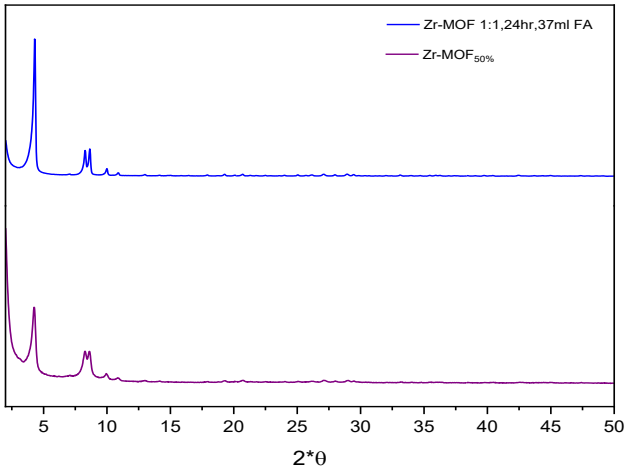

Figure 5.6: Diffractogram of samples with different Formic acid amounts

The diffractogram shows a clear decrease in peaks' intensities at 4.2, 9.98°, and 10.9° for the Zr-MOF$_{50\%}$ sample which can suggest a decrease in the concentration in the diffracting planes of the reported peaks in section 5.3.1. Moreover, further characterization using Unitcell Software shows a drop in crystallite size by more than half and an increase in the cell lattice constants as reported in Table 5.6.

Table 5.6: XRD data obtained from diffractograms

Sample code	Cell parameter(Å)	Cell volume(Å^3)	Crystallite size (Å)
Zr-MOF$_{50\%}$	35.59983	45117.37	404
Zr-MOF 1:1,24hr,37ml	35.46972	44624.59	1216

It can be concluded that acid modulators tend to promote the crystal growth of MOF. This is achieved by slowing down the reaction kinetics, thereby facilitating the formation of the nodes and preventing the fast precipitation of disordered or amorphous products. Also, this might be due to solubility issues because a lower formic acid content decreases the quantity of BTC dissolved in solution[76].

The effect of reducing formic acid volume on the textural properties is also to be assessed by N_2 adsorption measurement.

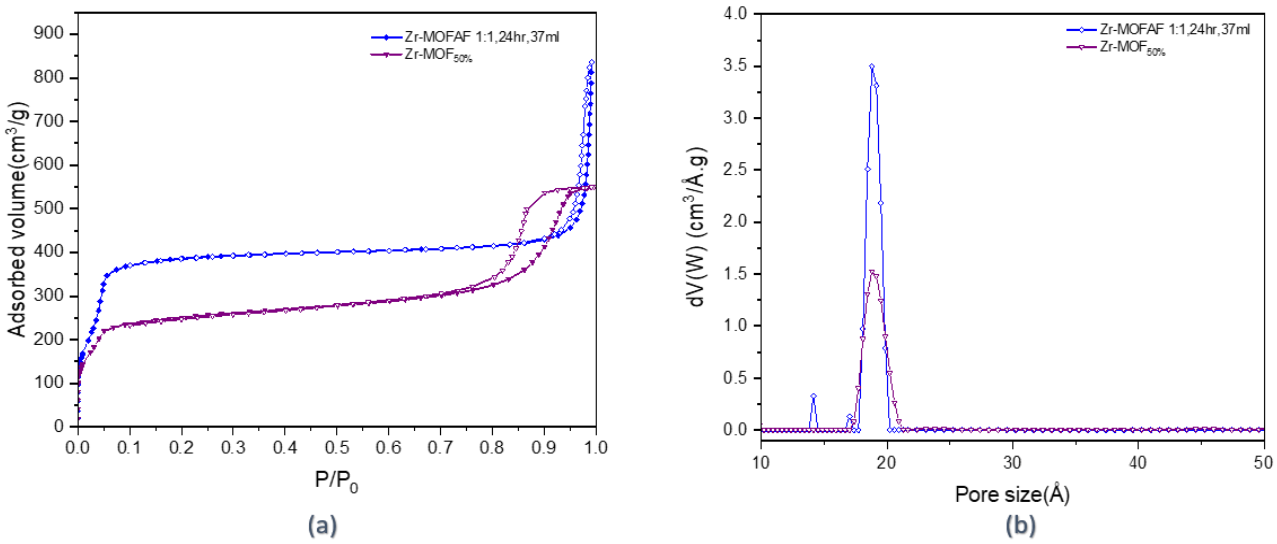

Figure 5.7: Different Formic acid volume (a)N_2 Adsorption-Desorption isotherms (b)Pore size distribution

Table 5.7: Data obtained from N_2 isotherms

Sample code	BET(m^2/g)	Total pore volume(cm^3/g)	Microporous area(m^2/g)	Microporous volume(cm^3/g)	Langmuir Area (m^2/g)
Zr-MOF50%	924	0.849	478.94	0.2012	1147
Zr-MOF 1:1,24hr	1475	1.294	906.7990	0.362271	1747

A notable change in the adsorption behavior of MOF-808 was observed when varying the Formic acid amount in the synthesis phase. In Figure 5.7(a), the isotherm describing the sample with half formic acid amount is a combination between type I and type IV isotherm, showing a steep increase in the adsorbed volume up to 150 cm3/g with a relative pressure varying from 0 to 0.05 that corresponds mainly to microporous monolayer coverage. A knee-shaped curvature is observed for a relative pressure just greater than 0.05 which indicates the completion of monolayer coverage and the beginning of multi-layer adsorption. The curve then shows a slight increase in the adsorbed volume up to P/P0=0.8 corresponding to the mentioned multi-layer coverage of the mesoporous region. A sudden increase is then shown with a hysteresis of type H2 that is related to nitrogen filling taking place in disordered mesopores having ink-bottle-shaped arranged pores. The plateau that is shown for relative pressure higher than 0.95 is related to pore condensation phenomenon[77]. Much lower nitrogen uptake is seen for the half formic acid sample which is consistent with the reported area values in Table 5.7.

In Figure 5.7(b), pore distribution shows only the pore at 18Å which is a characteristic of the MOF-808, with a significant drop in the intensities of the whole other peaks. It can be concluded that the use of less formic acid amount triggers a change in the typology and connectivity of the pores, lower surface area, and a disturb in the pore size distribution. This hypothesize the production of a less ordered and structured material.

The thermal stability of Zr-MOF$_{50\%}$ is also assessed and compared with the reference sample in Figure 5.8.

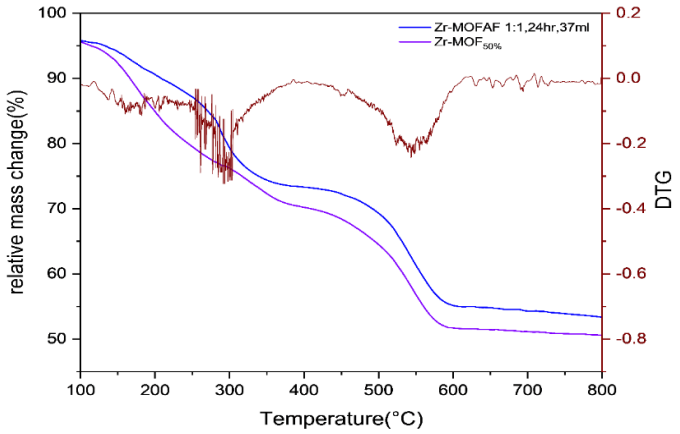

Figure 5.8: Thermo-grams of reference sample versus sample synthesized with half Formic acid volume

Table 5.8: Data obtained from thermos-grams

Sample code	Total weight loss(%)	Solvent weight loss(%)	Organic weight loss(%)
Zr-MOF 1:1,24hr,37ml FA	46.67	4.2	26.49
Zr-MOF$_{50\%}$	49.44	4.39	25.41

Both thermograms show the same thermal trend over the temperature range and approximately the same weight losses as reported in Table 5.8. It can be concluded that the difference in surface areas and crystallinity has no significant effect on the thermal stability of the reduced formic acid sample.

5.3.3 Effect of different Precursors

Another synthesis was carried out to evaluate the effect of different precursor using zirconium-tetra Chloride as a precursor with a synthesis duration of 24 hours. By using zirconium tetra-chloride we can also investigate the role of water molecules in the zirconium precursors on the final characteristics of the MOF. The synthesized sample is named Zr-MOF$_{ZrCl4}$.

The diffractogram of the sample synthesized with $ZrCl_4$ shown in Figure 5.9 shows a drop in the intensity of the 1st main peak at 4.2°. The peaks at 8.24°, 8.66°, are still present but with a different intensity ratio. Further extraction of data from diffractograms shows a drop in the crystallite size and an increase in cell parameters as reported in Table 5.9.

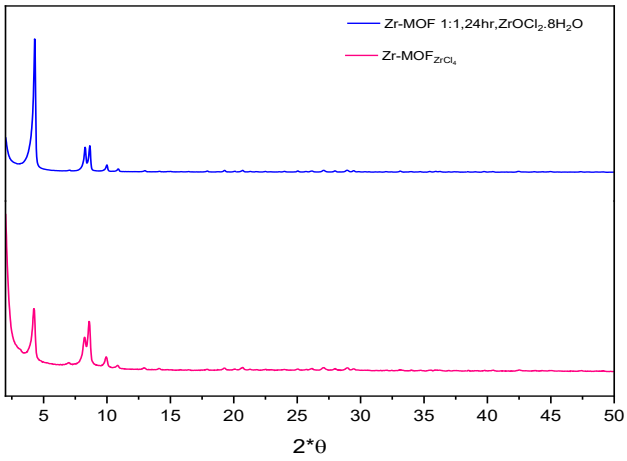

Figure 5.9: Diffractogram of samples with different precursors used

Table 5.9: XRD data obtained from diffractograms

Sample code	Cell parameter(Å)	Cell volume(Å^3)	Crystallite size (Å)
Zr-MOF 1:1,24hr	35.46972	44624.59	1216
Zr-MOF$_{ZrCl4}$	35.59983	45117.37	563

Ragon et. al[78] established that water may enhance the kinetics of crystallization of Zr-based MOFs. Water present in the $ZrOCl_2.8H_2O$ precursor favors the formation of Zr^{4+}oxo/hydroxo clusters hence boosting the crystallization rate. The decrease in crystal size can be related to the insufficient time needed for the formation of well-ordered crystals.

The effect of the used precursors on the textural properties is illustrated in Figure 5.10.

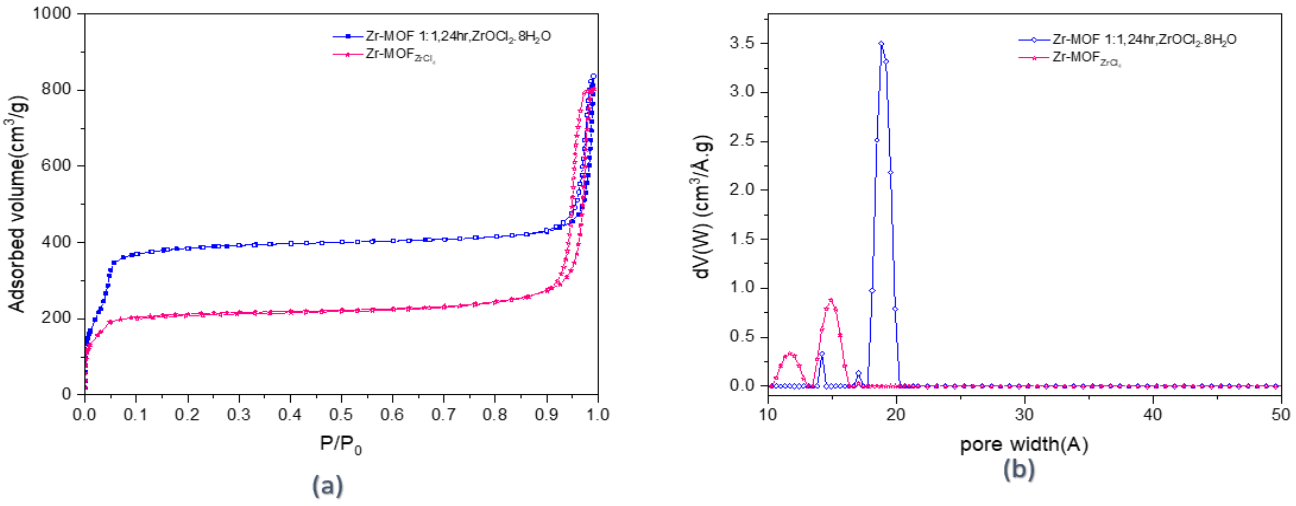

Figure 5.10: Different Precursors used (a)N_2 Adsorption-Desorption isotherms (b) Pore size distribution

Table 5.10: Data obtained from N_2 isotherms

Sample code	BET(m^2/g)	Total pore volume(cm^3/g)	Microporous area(m^2/g)	Microporous volume(cm^3/g)	Langmuir Area (m^2/g)
Zr-MOF$_{ZrCl4}$	804	1.236	511.74	0.2078	968
Zr-MOFAF 1:1,24hr	1475	1.294	906.7990	0.362271	1747

In Figure 5.10(a), the isotherms follow the same characteristics of type I and type IV with mild hysteresis. The description of the isotherm is identical to the one reported in section 5.3.1 Effect of Synthesis TimeThe lower nitrogen uptake is confirmed in the decrease in BET and Langmuir areas that are reported in Table 5.10.

Zirconium Chloride induces a disturbance in the pore size distribution leading the formation of a new curve's profile. A new pore peak at 13 Å is observed, while the peak at 18 Å disappear.

It can be concluded that the use of Zirconium Chloride as precursors induces a significant change in the pore typology, resulting in a lower surface area and different pore distribution.

Further assessment of the thermal stability of the synthesized sample is reported and compared with the reference sample. Both thermograms show the same thermal trend over the temperature range and approximately the same weight losses as reported in Table 5.11. It can be concluded that the difference in surface areas and crystallinity have no significant effects on the thermal stability of the sample synthesized with Zirconium-tetra Chloride.

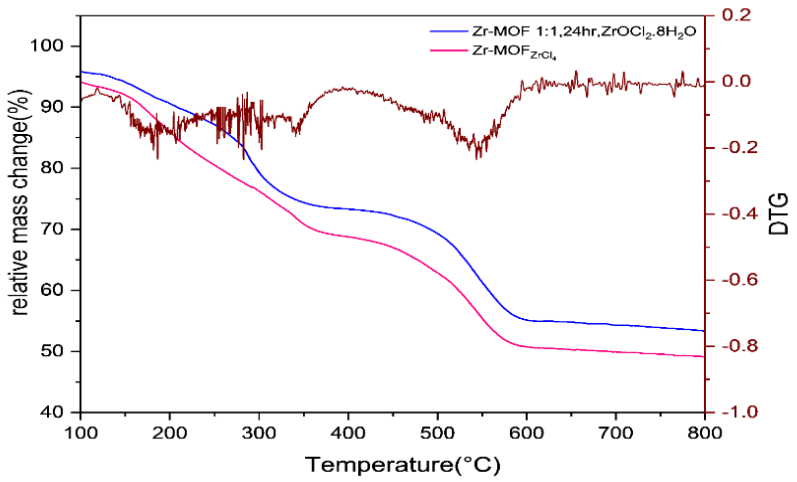

Figure 5.11: Thermo-grams of reference sample versus sample synthesized with $ZrCl_4$ precursors

Table 5.11: Data obtained from Thermograms

Sample code	Total weight loss(%)	Solvent weight loss(%)	Organic weight loss(%)
Zr-MOF 1:1,24hr	46.67	4.2	26.49
Zr-MOF$_{ZrCl4}$	50.87	5.85	25.38

Results summary

The following bargraph in Figure 5.12 shows the difference in properties between the formic acid sample Zr-MOFAF 1:1, 24hr reported in section 5.3.1 Effect of Synthesis Timeused as a benchmark and the other two derived samples which are Zr-MOF$_{50\%}$ and Zr-MOF$_{ZrCl4}$.

As mentioned in the plots above, an obvious drop in crystallinity and surface area is observed for the Zr-MOF$_{50\%}$ and Zr-MOF$_{ZrCl4}$. The calculation of defects concentration shows a drop although it wasn't clearly shown in the reported thermograms in Figure 5.8 and Figure 5.11. The results are reported in the graph below.

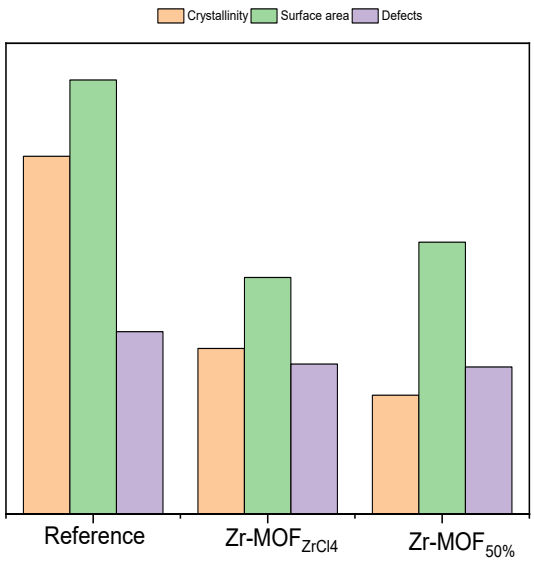

Figure 5.12: Results summary of samples synthesized with half formic acid amount and with $ZrCl_4$ precursors with respect to the reference sample

5.3.4 Effect of the zirconium precursors /BTC ligand ratio

Another important parameter to be assessed is the molar ratio between the Zirconium precursors and the BTC ligand. Different literature studies showed the ability to tune the MOF

properties by using different molar ratios[74]. Experiments were carried out under the same synthesis protocol mentioned in section 5.1 Synthesis Protocol using a molar ratio=3:1, where this ratio is reported to give an effective MOF-808 synthesis using acetic acid, with no previous assessment of the efficiency when used with formic acid as a modulator.

Three samples were synthesized with different synthesis times, where a comparison is carried out among the samples to assess the effect of synthesis time, and another comparison is carried out with respect to formic acid samples synthesized with a molar ratio=1:1 reported in section 5.3.1.

Table 5.12: Samples synthesized with molar ratio 3:1 under different synthesis time

Sample code	Molar ratio (Zr/BTC)	$ZrOCl_2.8H_2O$ (M)	BTC (M)	Acid volume(ml)	Temp (°C)	Time (h)
Zr-MOFAF 3:1,72hr	3:1	0.093	0.0312	37	110	72
Zr-MOFAF 3:1,48hr	3:1	0.093	0.0312	37	110	48
Zr-MOFAF 3:1,24hr	3:1	0.093	0.0312	37	110	24

As a first characterization implemented, the crystal parameters of the samples were retrieved from XRD data.

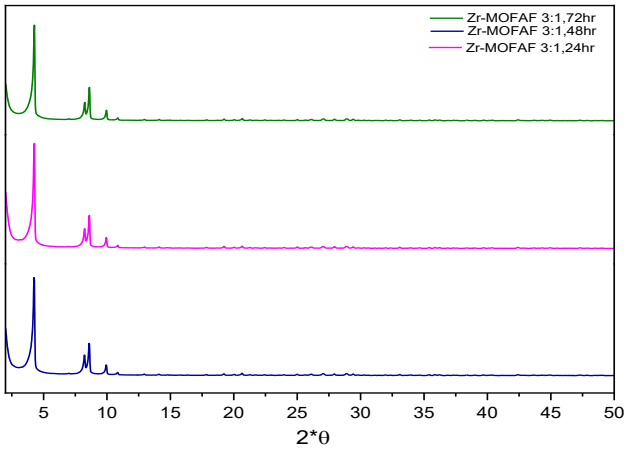

Figure 5.13: Diffractograms of Samples synthesized with molar ratio 3:1 under different synthesis time

No evident variation in the diffractogram patterns where all the main peaks are present. Higher intensity of peaks at 8.66° and 9.98°are shown in Figure 5.13 compared to samples synthesized with a 1:1 molar ratio represented in Figure 5.1. Also, a long synthesis time may have led to the reorganization of the materials with the same trend in textural properties. This is observed in the lower nitrogen uptake of the 72 hours treated sample and drop in microporous peak intensities in Figure 5.14. Further extraction of data evidence the formation

of smaller crystallites compared to those obtained with Zr precursor/ BTC= 1:1. These findings may be linked to the excessive amount of zirconium precursor in this particular synthesis reaction.

Table 5.13: XRD data obtained from diffractograms

Sample code	Cell parameter(Å)	Cell volume(Å³)	Crystallite size (Å)
Zr-MOFAF 3:1,72hr	35.60944	451153.92	1228
Zr-MOFAF 3:1,48hr	35.66987	45384.18	1268
Zr-MOFAF 3:1,24hr	35.63114	45236.52	1289

The effect of time variation on the textural properties of samples synthesized with Zr/BTC molar ratio=3:1 is represented in what follows.

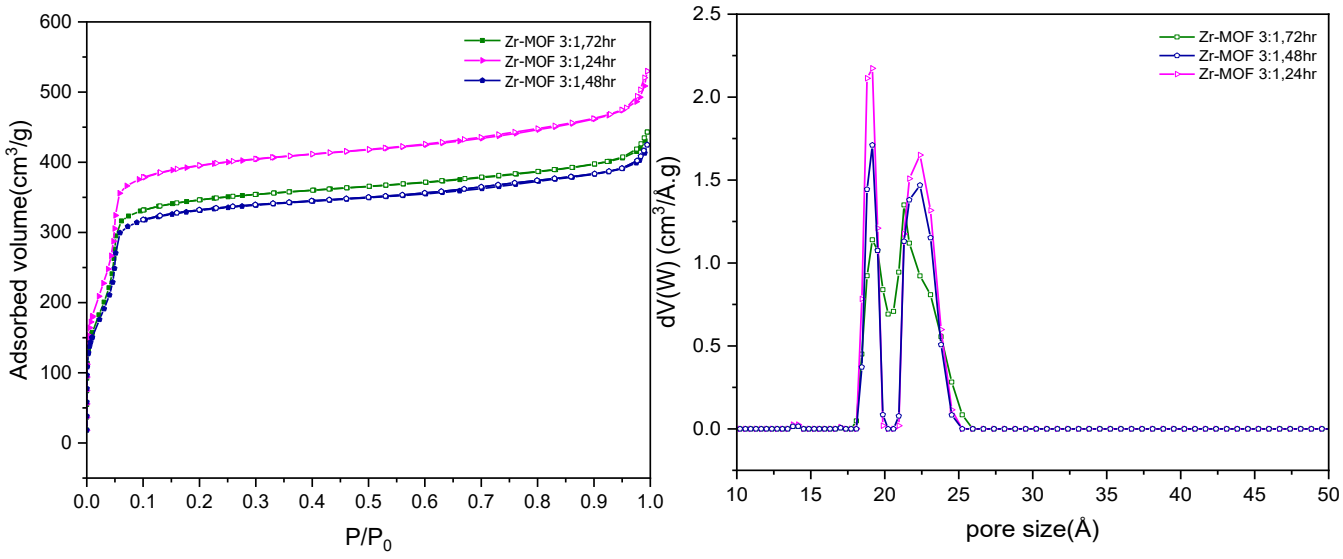

(a) *(b)*

Figure 5.14: Formic acid samples synthesized with molar ratio 3:1 with different synthesis time (a)N_2 Adsorption-Desorption isotherms (b)Pore size distribution

Table 5.14: Data obtained from N_2 isotherms

Sample code	BET(m²/g)	Total pore volume(cm³/g)	Microporous area(m²/g)	Microporous volume(cm³/g)	Langmuir Area (m²/g)
Zr-MOFAF 3:1,72hr	1312	0.663400	708.5516	0.2898	1577
Zr-MOFAF 3:1,48hr	1251	0.639507	744	0.3029	1510
Zr-MOFAF 3:1,24hr	1469	0.793574	804.0183	0.355701	1809

The N_2 adsorption isotherms under 77K exhibit mostly type IV as they show a continuous increase without reaching a plateau which suggests dominant mesoporous textures. A relatively abrupt increase in the adsorbed volume is registered for a relative pressure below 0.1, which corresponds to the adsorption in microporous regions.

Samples synthesized with Zr/BTC=3:1 possess the same pore size distribution observed in Figure 5.3(b) but at a lower intensity in the microporous region and higher intensity in the mesoporous region. This can show that the inverted ratio triggered more mesoporous textures which are confirmed by the obtained isotherms. The higher nitrogen uptake of the 24 hours synthesized sample followed by the 72-hour treated sample and then the 48 shown in Figure 5.14 follows the same trend regarding BET and Langmuir are reported in Table 5.14. Moreover, the higher the intensity of the microporous peak at 18Å appears the higher the microporous area of the sample.

The thermal stability of the samples is characterized by TGA analysis which allows further determination of other characteristics such as defects. The obtained curves are presented inFigure 5.4.

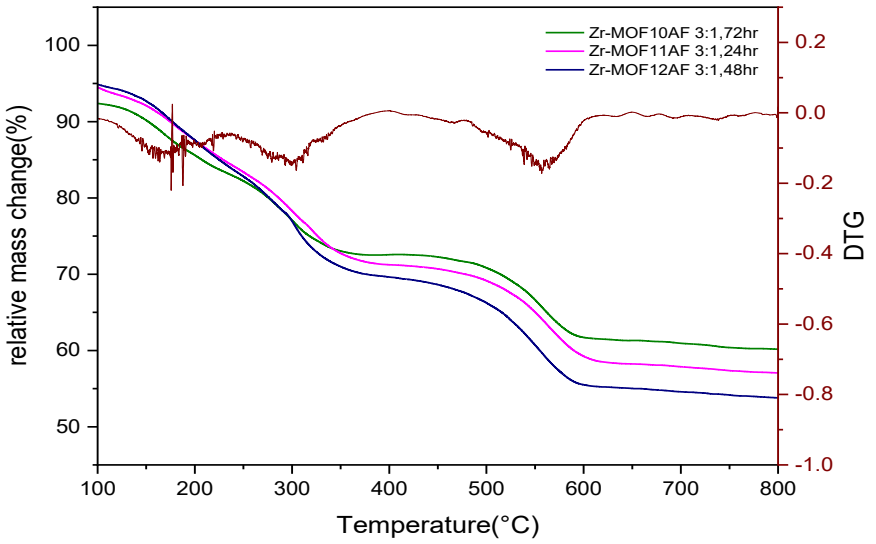

Figure 5.15: Thermo-grams and DTG plots of Formic acid samples synthesized with molar ratio 1:1 with different synthesis times.

Table 5.15: Data obtained from Thermograms

Sample code	Total weight loss(%)	Solvent weight loss(%)	Organic weight loss(%)
Zr-MOFAF 3:1,72hr	39.83	7.61	21.55
Zr-MOFAF 3:1,48hr	46.21	5.12	28.36
Zr-MOFAF 3:1,24hr	43.02	6.37	25.09

Results summary

It can be shown that the highest surface area is obtained for the sample synthesized with 24 hours of treatment, with conserved crystallinity and defects concentration among all the samples. All the samples seem of interest for further catalytic application.

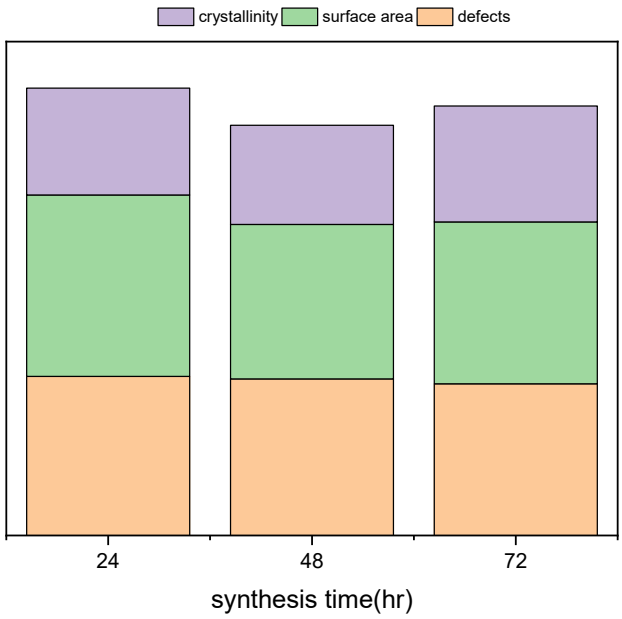

Figure 5.16: Results summary of Formic acid samples synthesized with molar ratio 3:1 with different synthesis time

Characteristics Summary of all samples synthesized with Formic acid

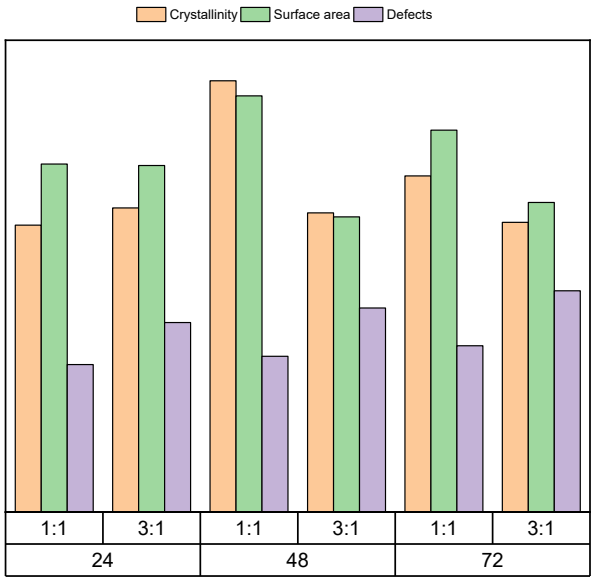

Figure 5.17: Characteristics summary Formic acid samples synthesized with a 3:1 molar ratio versus Formic acid samples synthesized with a 1:1 molar ratio

A slight decrease in the surface area and crystallinity is reported for samples synthesized with Formic acid with a molar ratio=3:1 which can be due to the high amount of Zirconium salts that lead to non-efficient interaction between reagents.

A noticeable increase in the percentage of defects in the samples with a 3:1 molar ratio. Although the mechanism of this effect on the formation of missing linkers is still unclear, it is possible to propose that the rate of SBU formation is accelerated by the excessive amount of zirconium precursor and increases the competition to assemble with a more limited number of organic linkers[74]. This may explain the decreased crystallinity of samples synthesized with a molar ratio of 3:1 than samples synthesized with a molar ratio=1:1.

The textural properties results support also the TGA analysis because samples synthesized with acetic acid that show lower surface area, also show fewer number of defects[75].

5.4 Acid Modulator Effect: Samples Synthesized with Acetic Acid

In the following section, all the samples synthesized with acetic acid are presented. The variation in synthesis time, acetic acid volume, and the molar ratio are explored.

In Figure 5.18, XRD patterns of samples synthesized with acetic acid with a molar ratio Zr/BTC=3:1 under different synthesis time are reported.

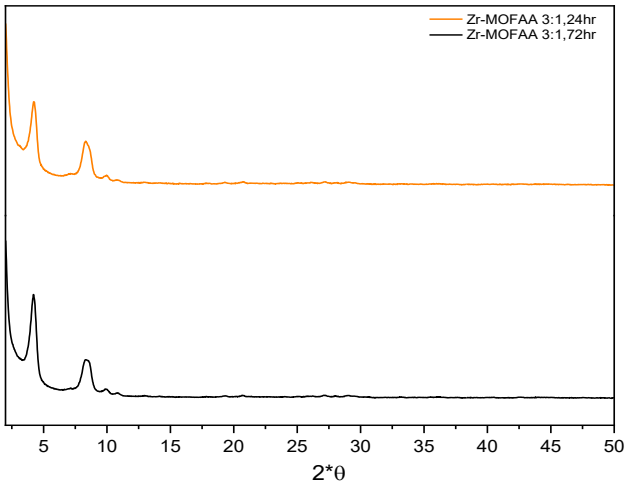

Figure 5.18: Diffractograms of Samples synthesized with molar ratio 3:1 under different synthesis time

Compared to samples synthesized with formic acid, the peaks defined at 8.24° and 8.66° seem to be merged, whereas the peaks defined at 9.98° and 10.9° are hardly distinguishable from the background of the diffractogram. This indicates the non-effectiveness of the role of acetic acid as a modulator in MOF-808 synthesis [79].

Table 5.16: XRD data obtained from diffractograms

Sample code	Cell parameter(Å)	Cell volume(Å^3)	Crystallite size (Å)
Zr-MOFAA 3:1,72hr	35.56221	44974.49	163
Zr-MOFAA 3:1,24hr	35.47415	44641.20	182

A further investigation of the crystallinity parameters shows a drop in the crystallinity size and an increase in cell parameters with increasing synthesis time as shown in Table 5.16. The lower intensity of the main peaks shown in Figure 5.18 accompanied by drop in crystallinity size in Table 5.16 with respect to the crystallite size of samples synthesized with formic acid can suggest that we are shifting toward a more amorphous product.

The morphology of selected sample synthesized with acetic acid is to be assessed by SEM.

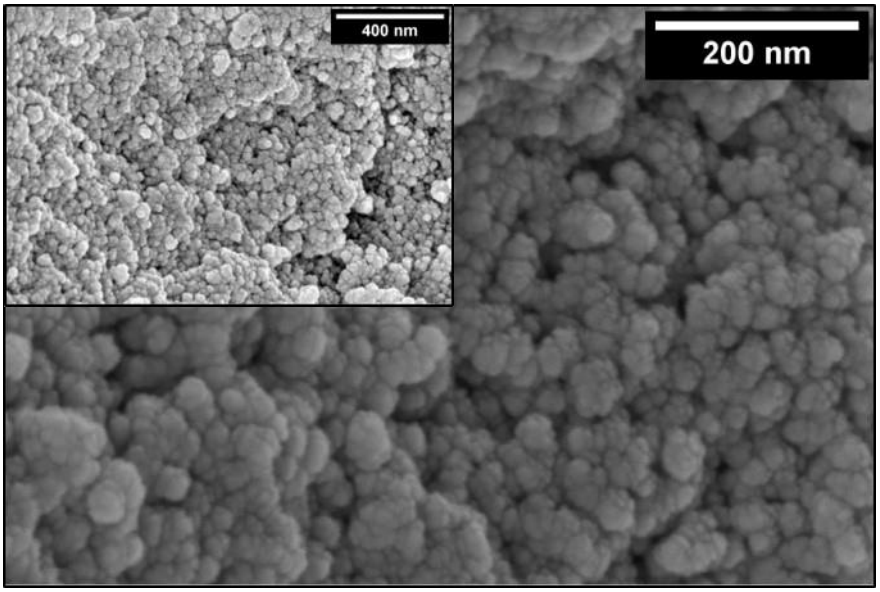

Figure 5.19: SEM Micrographs of MOF samples with acetic acid, molar ratio Zr: BTC 3:1 72h. In the insert is reported the wide view.

The micrograph of sample Zr-MOF AA 3:1, 72h shows a distribution of smaller nanoparticles, compared with formic acid samples, and with a more spherical shape.

A further assessment of N_2 adsorption analysis is carried out in the following section to address the effect of different synthesis times on the textural development for MOF-808 synthesized using acetic acid.

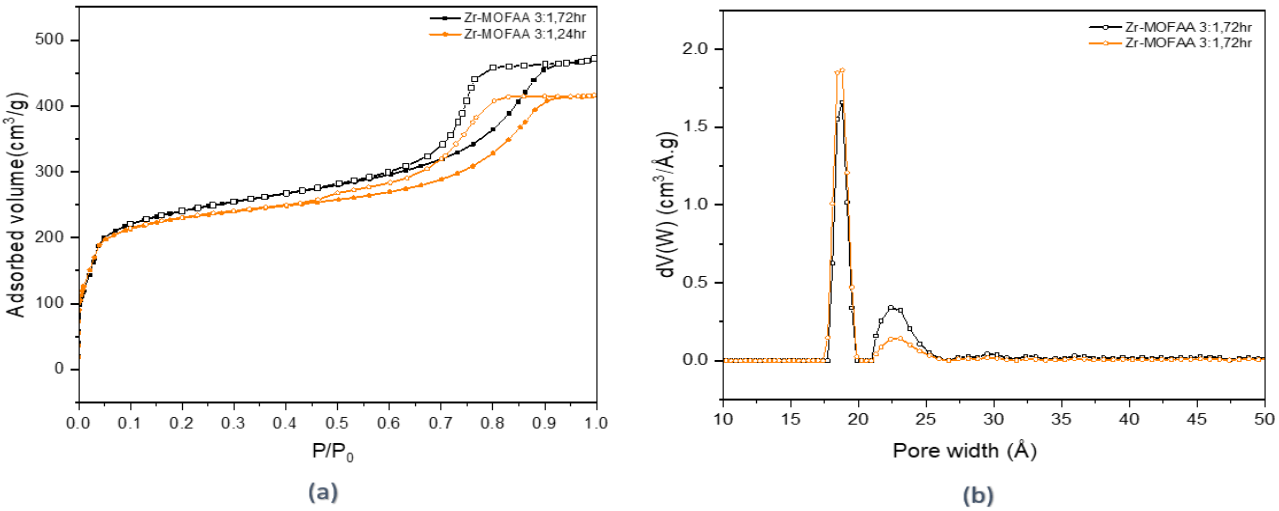

Figure 5.20: Acetic acid samples synthesized with molar ratio 3:1 with different synthesis time (a)N_2 Adsorption-Desorption isotherms (b)Pore size distribution

Table 5.17: Data obtained from N_2 isotherms

Sample code	BET(m^2/g)	Total pore volume(cm^3/g)	Microporous area(m^2/g)	Microporous volume(cm^3/g)	Langmuir Area (m^2/g)
Zr-MOFAA 3:1,72hr	862	0.731	290	0.130	1146
Zr-MOFAA 3:1,24hr	829	0.642	381	0.164	1086

The isotherm in Figure 5.20 exhibits a combination between type I and type IV isotherms. The isotherm shows steep adsorption up to 200cm^3/g for a relative pressure of P/P_0=0.1 corresponding to monolayer coverage in micropores. Then it is followed by an increase in the adsorbed volume up to a relative pressure P/P_0=0.8 which corresponds to the mesopores multi-layer filling. An H2 type hysteresis is shown at the end followed by a plateau adsorption that was also shown and explained in Figure 5.7. Same Isotherm trend and hysteresis can suggest the same pore typology and connectivity among these samples.

Higher nitrogen uptake is seen for the sample synthesized within 72hours which is also confirmed in higher BET and Langmuir areas in Table 5.17. Moreover, it can be seen on average, that the values of the BET and Langmuir area decreased to the half almost when using acetic acid as a modulator in the synthesis compared to samples synthesized with formic acid (Table 5.4).

The pore distribution follows the same trend for the two samples showing a major peak at 18 Å and other mesoporous distribution centered at 23.3 Å. The sample synthesized within 72hours shows an evident lower microporous peak intensity and higher mesoporous peak which can be related to the dissolution upon treatment with long duration is also confirmed in the decreased crystallinity size in Table 5.16. That is to say that the mesoporosity of the acetic acid is related to the presence of amorphous products. The intensity of the microporous decrease and mesoporous peaks increases as the time of synthesis increases.

It is observed that samples synthesized with acetic acid show much less developed microporous peaks where the peaks at 14Å and 17Å are not observed in samples synthesized with acetic acid (Figure 5.20) in contrast to samples synthesized with formic acid(Figure 5.3). Also it is shown a drop in the peak intensity at 18 Å in acetic acid samples almost to half with respect to the same peak intensity for formic acid samples.

Compared to samples synthesized with formic acid, the use of acetic acid in synthesis shows to induces different and narrower pore distribution, different pore types, and lower surface area than samples synthesized with formic acid.

Another set of synthesis with a Molar ratio=1:1 that resulted in developed MOF-808 synthesis in section 5.3.1 Effect of Synthesis Time when carried with Formic acid, is carried out but with the use of Acetic acid, as these conditions are not studied in the literature.

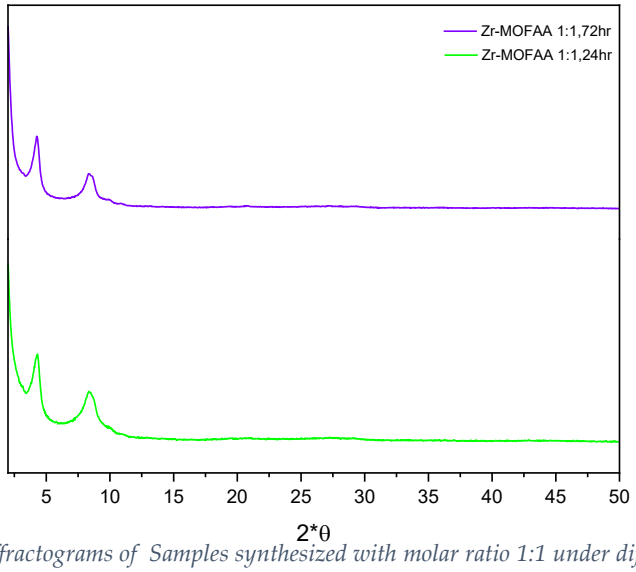

Figure 5.21: Diffractograms of Samples synthesized with molar ratio 1:1 under different synthesis time

Table 5.18: XRD data obtained from diffractograms

Sample code	Cell parameter(Å)	Cell volume(Å^3)	Crystallite size (Å)
Zr-MOFAA 1:1,72hr	35.46455	44604.98	161
Zr-MOFAA 1:1,24hr	35.73306	45625.81	117

The same notes mentioned in section 5.4 Acid Modulator Effect: Samples Synthesized with Acetic Acid about diffractograms are applied here. However with samples synthesized with a 1:1 molar ratio, the crystal size increases as time increases as shown in Table 5.18, which is also confirmed in the higher peak intensity at 18 Å of the 72hours treated sample shown in Figure 5.22.

Also, it is noticed that the crystallinity size for samples synthesized within 72hours shows almost similar values for different molar ratios. However, a decrease in the crystallinity is shown for the sample synthesized for 24 hours under a molar ratio=1:1 than ones synthesized with a molar ratio=3:1 (Table 5.16, Table 5.18). Higher crystallite size is observed for higher Zr/BTC ratio samples in Table 5.16 that can be attributed to the higher metal-ion portion that leads to an easier collision of organic BTC molecules and further better coordination between Zr^{4+} ions with BTC molecules[67].

A further assessment of N_2 adsorption analysis is carried out in the following section to address the effect of different synthesis times on the textural development for MOF-808 synthesized using acetic acid with a molar ratio Zr/BTC=1:1.

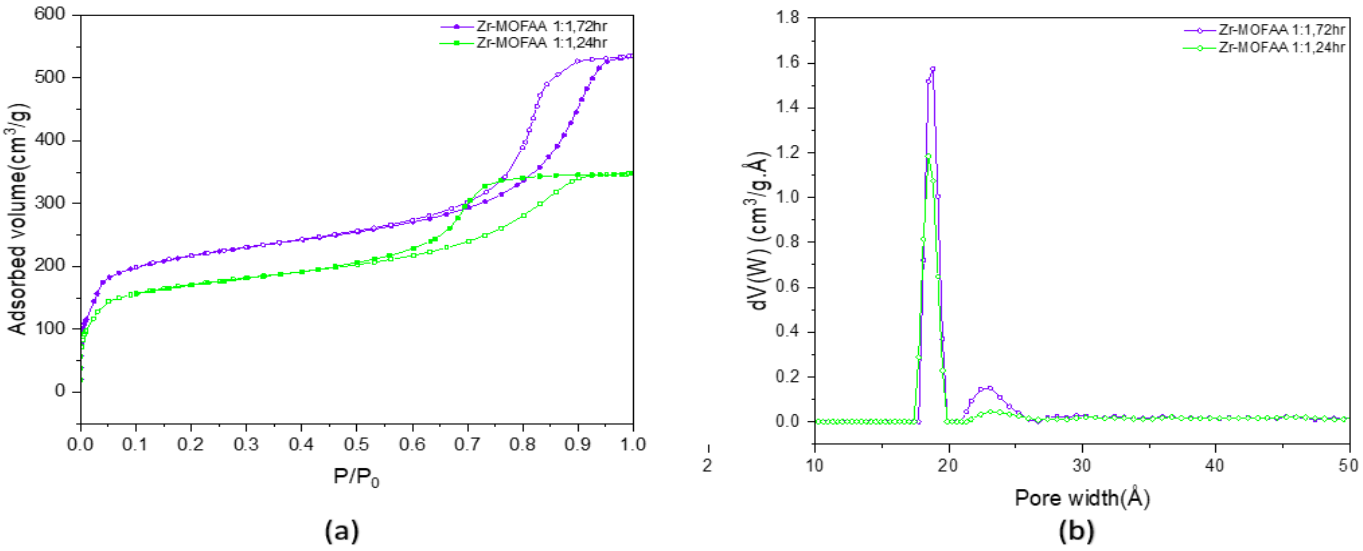

Figure 5.22: Acetic acid samples synthesized with molar ratio 1:1 with different synthesis time (a)N2 Adsorption-Desorption isotherms (b)Pore size distribution

Table 5.19: Data obtained from N_2 isotherms

Sample code	BET(m^2/g)	Total pore volume(cm^3/g)	Microporous area(m^2/g)	Microporous volume(cm^3/g)	Langmuir Area (m^2/g)
Zr-MOFAA 3:1,72hr	782	0.826	282	0.123276	1034
Zr-MOFAA 3:1,24hr	588	0.539	200	0.099197	798

The same analysis is carried out for the isotherms in Figure 5.22 as the ones in Figure 5.20(a). The pore distribution follows the same trend for the two samples showing a major peak at 18 Å and other mesoporous distribution centered at 23.3 Å. The sample synthesized with 72hours shows a higher microporous mesoporous peak intensity which is also confirmed in the increased crystallinity of the 72-treated hour sample shown in Table 5.18.

Further assessment of the thermal stability is carried out on the synthesized samples. Both thermograms show the same trend over the temperature range and approximately the same weight losses as shown Table 5.20. The acetic acid sample shows roughly a constant slope decline without any transition phase between region II and region III. A drop in the percentage of defects is observed in the acetic acid samples with respect to samples synthesized with formic acid.

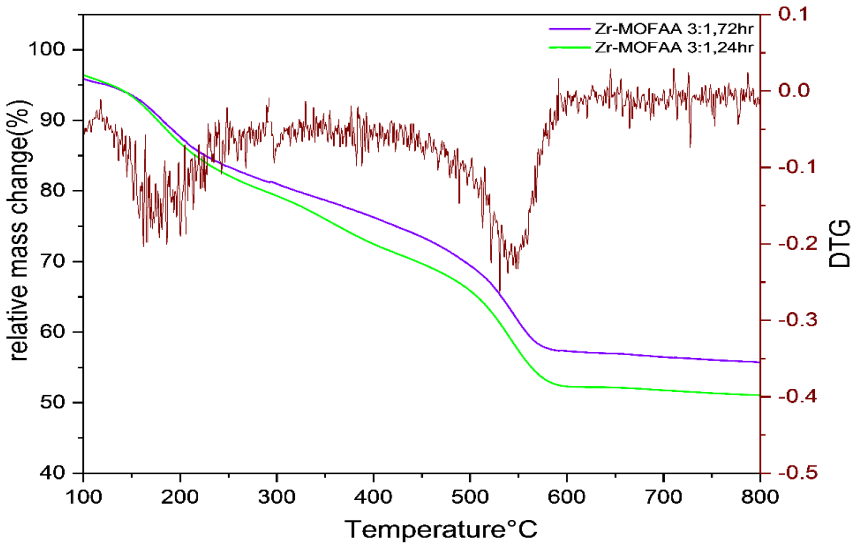

Figure 5.23: Thermo-grams and DTG plots of Acetic acid samples synthesized with molar ratio 1:1 with different synthesis times.

Table 5.20: Data obtained from thermo-grams

Sample code	Total weight loss(%)	Solvent weight loss(%)	Organic weight loss(%)
Zr-MOFAA 1:1, 72hr	44.29907	4.09839	26.47841
Zr-MOFAA 1:1, 24hr	48.958	3.5777	30.558

Characteristics Summary

Decreasing the time of synthesis among samples synthesized with Acetic acid shows decreased overall properties, as crystallinity, surface area, and microporous area. But in general, all samples synthesized with Acetic acid show much lower characteristics with respect to samples synthesized using Formic acid, which renders them not of interest for any further catalytic applications. In addition, no samples were synthesized within 48 hours of a treatment since apparently, it will show roughly the same range of values which will keep being below the threshold needed for the catalytic test, so the two extreme durations (24 and 72 hours) were studied only.

Another synthesis was carried out with a sample containing half Acetic acid volume. The results show a complete collapse of the structure with no evidence of the development of targeted MOF-808.

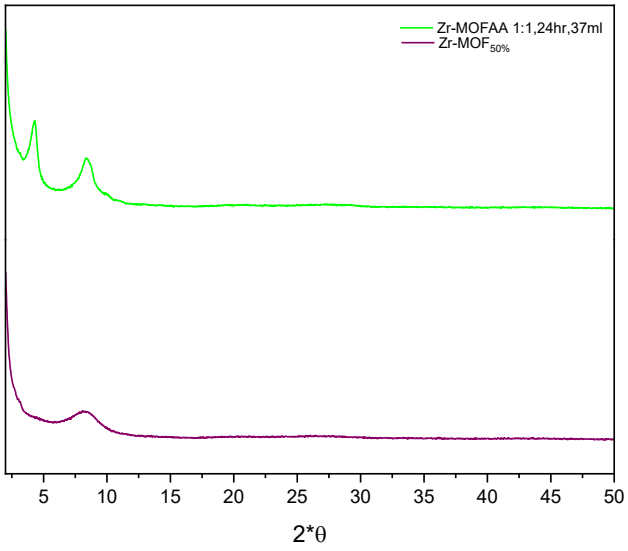

Figure 5.24: Diffractogram of samples with different Acetic acid amounts

No synthesis was carried out using $ZrCl_4$ as a precursor in an Acetic acid medium since both parameters result in a lower surface area and crystallinity.

Characteristics Summary between Formic acid samples versus Acetic acid samples

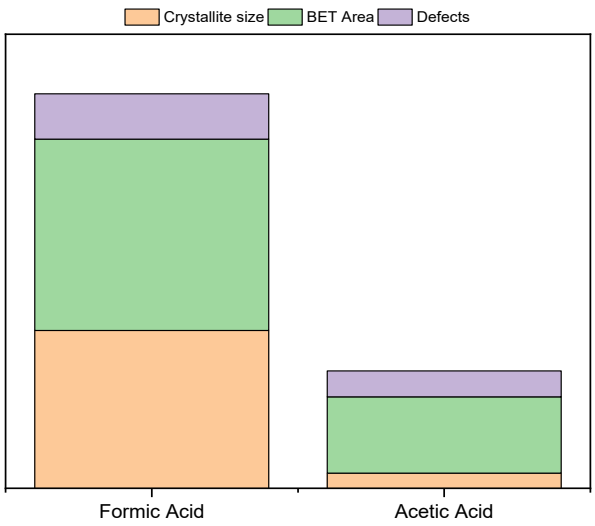

Figure 5.25: Summary of characteristics differences between Formic acid and Acetic Acid samples

Samples synthesized with Formic acid lead to a larger amount of defects which is consistent with the increased surface area and multiple pore peaks distributions. Modulators with higher pKa value (Acetic Acid) can form a stronger bond with Zr clusters, while modulators with lower pKa (Formic acid) values deprotonate easier, so a larger number of protons will be present in the synthesis solution that can suppress ligand deprotonation. These protons increase the difficulty of ligand deprotonation, so more defects are formed[80].

Also it can be seen from the lower number of pore peaks observed in samples synthesized with formic acid (Figure 5.3 and Figure 5.14) with respect to samples synthesized with acetic acid (Figure 5.20 and Figure 5.22).

Also it is shown that a decrease in the length of the carbon chain of the modulator leads to more developed pore structures with a larger surface area. When the same amount of modulator is added in the synthesis, a modulator with a lower pKa value leads to a higher surface area[72].

All samples show roughly the same total weight loss in the TGA analysis, however, samples synthesized with Formic acid tend to have higher thermal stability over the range 400°C-500°C.

Chapter 6 Catalytic Application

The catalytic tests were realized in collaboration with Prof. Vincenzo Russo at the Department of Chemical Sciences of the University of Naples Federico II.

Table 6.1: Chemicals used during the catalytic test

Product	CAS	Manufacturer
Methanol	67-56-1	Merck KGaA
Ethyl Levulinate	538-88-8	VWR,>99.8%

Reaction Procedure

The reaction is done in a glass flask batch reactor for 5 hours in a reflux manner at the boiling point of methanol (65°C). Methanol was added in excess with respect to Ethyl Levulinate with a ratio of 1:10 (mol/mol) with a catalyst loading of 0.5wt%.

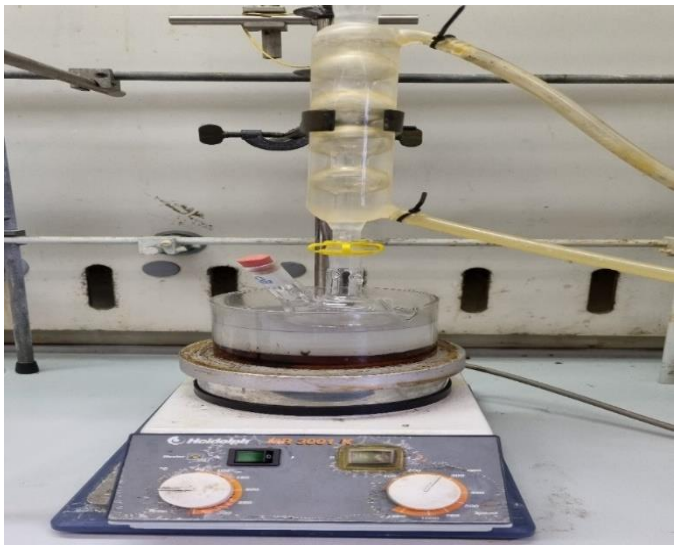

Figure 6.1: Catalytic reaction setup

Samples were taken at t = 0, 2.5 h, and 5 h, and the samples were analyzed by 1H-NMR. The test was done at the boiling point of methanol reaching 65°C.

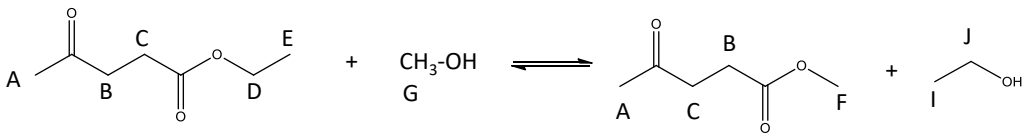

Figure 6.2: ML synthesis reaction from EL noting the different Hydrogen environments

Samples are analyzed by ^{1}H-NMR using $CDCl_3$ as solvent. Different Hydrogen environments are investigated to assess the conversion of Ethyl Levulinate into Methyl Levulinate. Hydrogen atoms marked as B and C cannot identify the efficient conversion into the products as they are Hydrogen environments that are present both in the reactants and product side. Moreover, the Hydrogen atom marked as E on the reactant side also shares the same chemical shift as the Hydrogen marked as I on the product side. So the relative intensities of these peaks cannot be calculated to determine the conversion since the decrease in intensity of these peaks at their specified chemical shift caused by the vanishing of the reactants, is compensated by the increase in their intensity due to the formation of the products. The vanish of the spectrum revealing Hydrogen D and the presence of new peaks shown by F and J can indicate the presence of our targeted Methyl Levulinate. The conversion of Ethyl Levulinate into Methyl Levulinate was calculated considering the signals of methyl groups resonating at a chemical shift of about 3.7 ppm (labeled with F) and by comparing with the integral of the signals of methyl groups resonating at a chemical shift of 2.2 ppm (labeled with A).

6.1 Catalytic Tests for Samples Synthesized with Formic Acid

Due to their promising properties, the first investigated samples were the samples synthesized with a molar ratio=1:1 using $ZrOCl_2.8H_2O$ as precursors which are mentioned in section 5.3.1 Effect of Synthesis Time given by 1) Zr-MOF AF 1:1,72hr 2) Zr-MOF AF 1:1,48hr 3) Zr-MOF AF 1:1,24hr

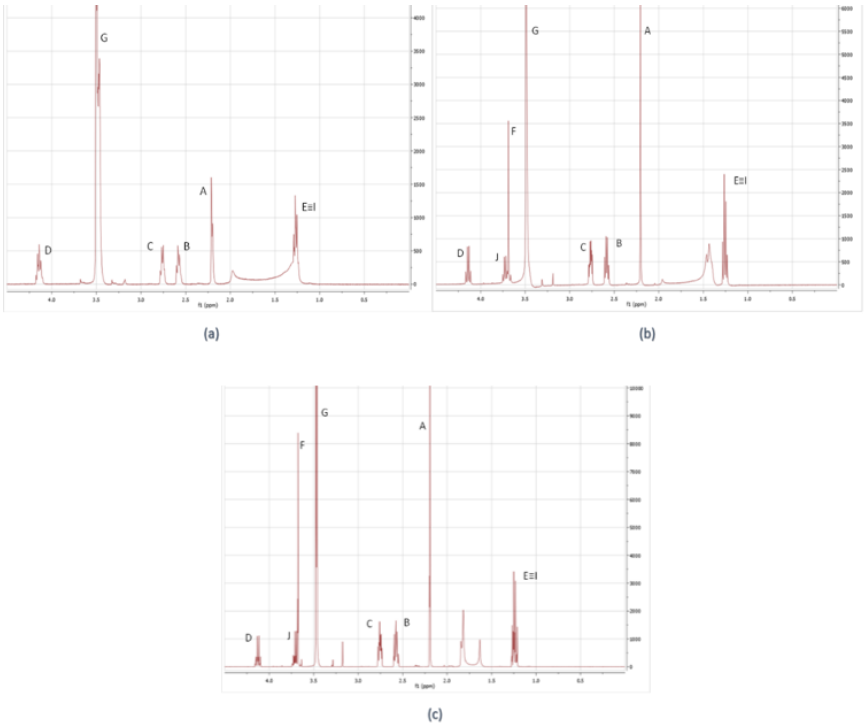

Figure 6.3:^{1}H NMR test of the reaction system using Zr-MOFAF 1:1,72hr at three different time (a)t=0 (b)t=2.5hr (c)t=5hr

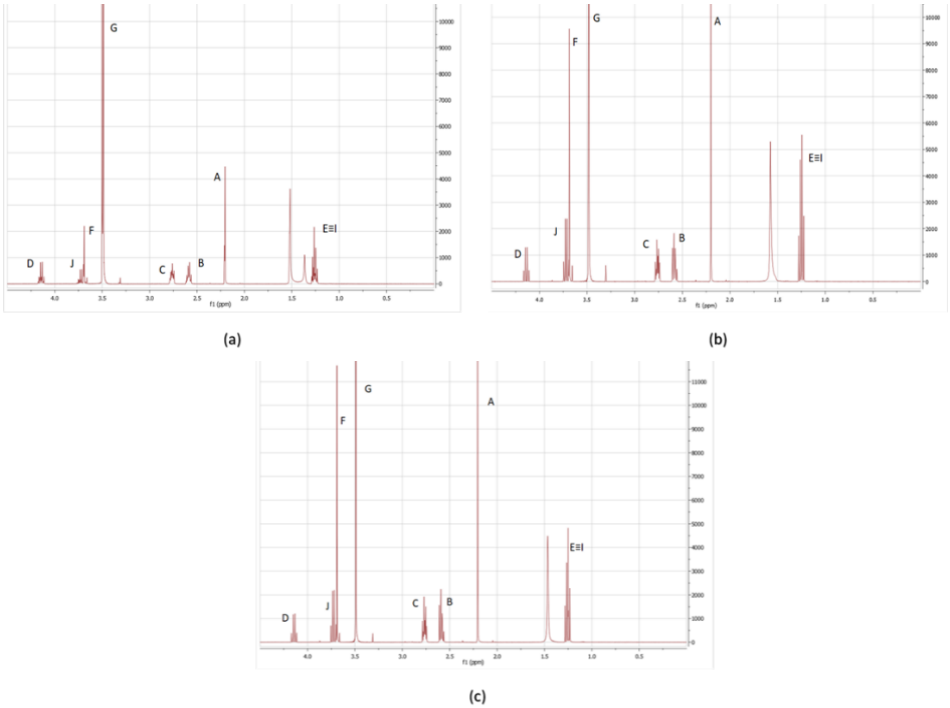

Figure 6.4: ^{1}H NMR test of the reaction system using Zr-MOFAF 1:1,48hr at three different time (a)t=0 (b)t=2.5hr (c)t=5hr

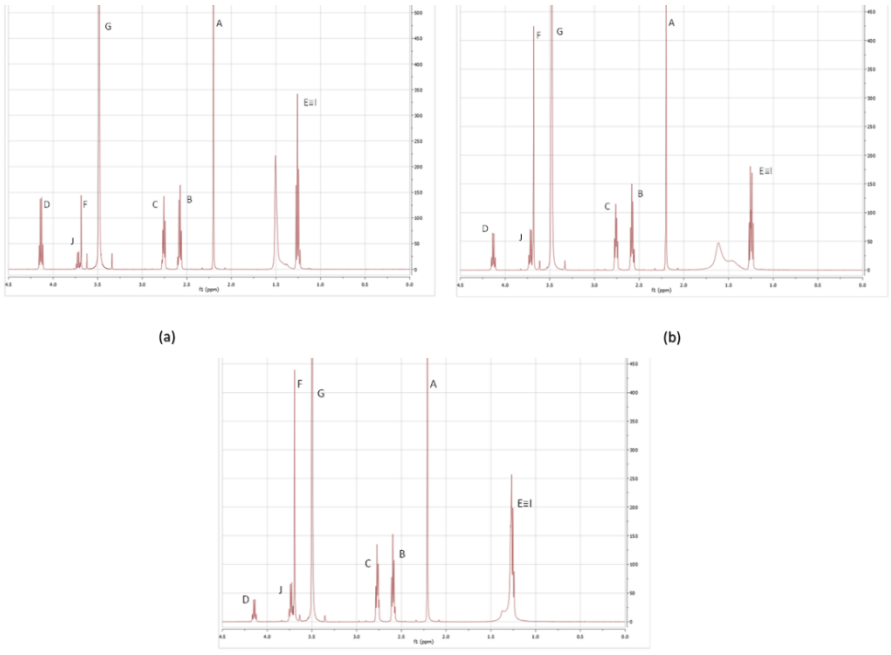

Figure 6.5:^{1}H NMR test of the reaction system using Zr-MOFAF 1:1,24hr at three different time (a)t=0 (b)t=2.5hr (c)t=5hr

The degree of conversion achieved (X) was calculated from the following normalized ratio for the number of protons responsible for the signals considered:

$$X = \frac{A_F}{A_A}$$

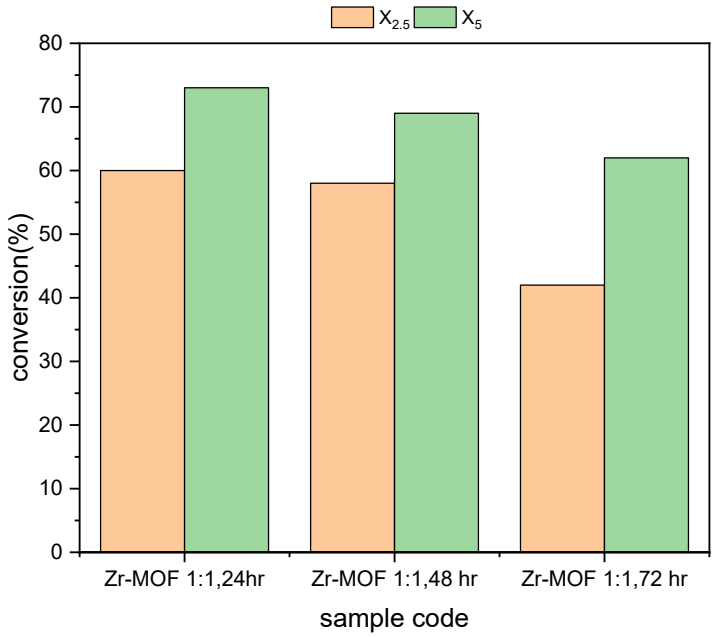

Figure 6.6: Reaction conversion summary for samples synthesized with formic acid

In general, it can be seen that the final conversion is increasing as the synthesis time decrease. Although there is not much differences between the properties investigated for these samples, the difference can be related to the vacant metal sites given by Lewis acidic sites that can increase the activity of the catalyst. The increased number of active sites enhances the reactivity regardless of the surface area.

The conversion reached by MOF-808 synthesized with formic acid records much higher values than classical acid catalysts that are traditionally employed in the synthesis of methyl levulinate shown in Chapter 4, Table 4.1 with much lower reaction temperature which escalates the importance of our synthesized MOF as energy saving material.

Table 6.2: Overview of reaction conditions for the conversion of biomass to ML using MOF-808

Raw material	Catalyst	Temperature(°C)	Reaction time(h)	Yield(%)
Ethyl Levulinate	MOF-808	65	5	73

6.2 Catalytic Tests for Sample Synthesized with Acetic Acid

In addition, although all samples synthesized with acetic acid shown in section 5.4 Acid Modulator Effect: Samples Synthesized with Acetic Acid has shown low properties that drive catalytic reactions effectively, a catalytic test was carried out to also assess the non-

presence of any non-covered properties that may cause different expected reaction conversion, which was confirmed in the test results below.

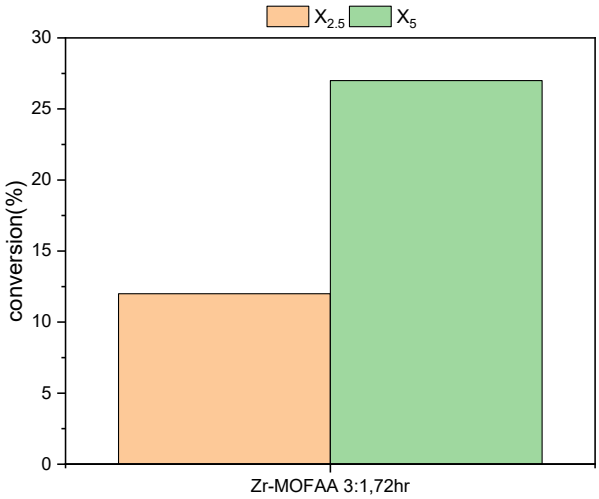

Figure 6.7: Reaction conversion summary for samples synthesized with acetic acid

Chapter 7 Stability Test

The promising results that are shown of the conversion results of MOF-808 samples synthesized with formic acid with respect to conventional acidic catalysts encourages catalytic studies of MOF-808 in other reactions conducted in different reagent mediums. For that, the stability test in different reagents was carried.

The chemical stability of the catalyst was investigated in different solutions to assess its structural resistance to solutions under different pHs. The amounts of the used reagents are reported in Table 7.1.

Table 7.1: Stability test conditions

	Solvent amount	MOF amount(g)	Concentration(mol/l)
Water stability	250ml	0.2	-
Acid stability HCl	100ml	0.15	1
Base stability NaOH	100ml	0.15	1

Stability test Procedure

MOF is added to a 1M concentration solution obtained by dilution into a round bottom flask, immersed in an oil bath having a constant temperature of 30°C, and left stirring at 50RPM for 24 hrs. The solution is then centrifuged and filtered with acetone under a vacuum setup. Then it is left to dry in the oven for 1hr at 70°C.

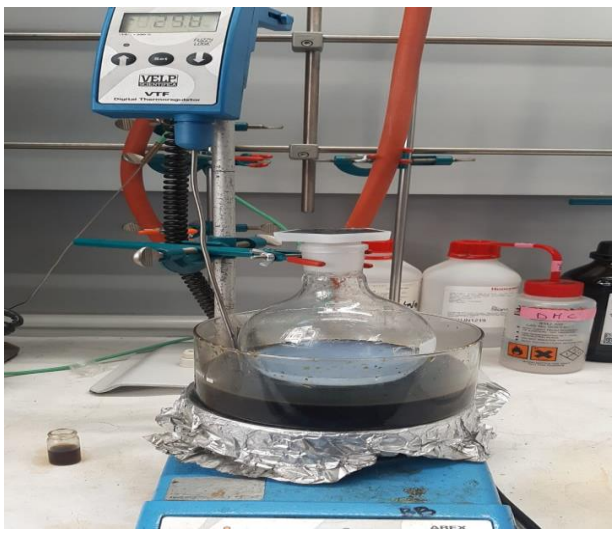

Figure 7.1: Stability test setup

The catalyst Zr-MOFAF 1:1,72hr was chosen to conduct a stability test in different solutions. Stability in water and acid are of high interest for catalysts in biomass reactions since they are

usually present as byproducts in most of the reactants. The accurate assessment of the stability in such mediums can prevent further leaching effects on the catalyst. Moreover, all the catalysts were washed with methanol during synthesis, which suggests additional stability to the leaching effect in the reaction system.

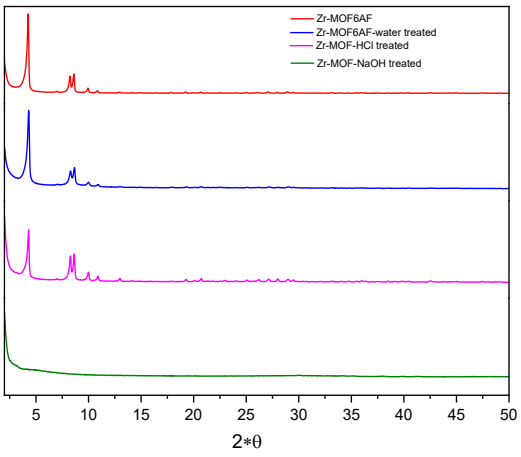

Figure 7.2: Diffractograms of the treated samples

The treatment of the sample in water and acid didn't affect the crystalline structure, however, it shows a complete collapse of the structure when treated with NaOH. The MOF-808 is not stable in the NaOH solution, for which the reason may be that the OH^- ion has a strong coordination ability to destroy the Zr–O coordination bond for the formation of zirconium hydroxide[67].

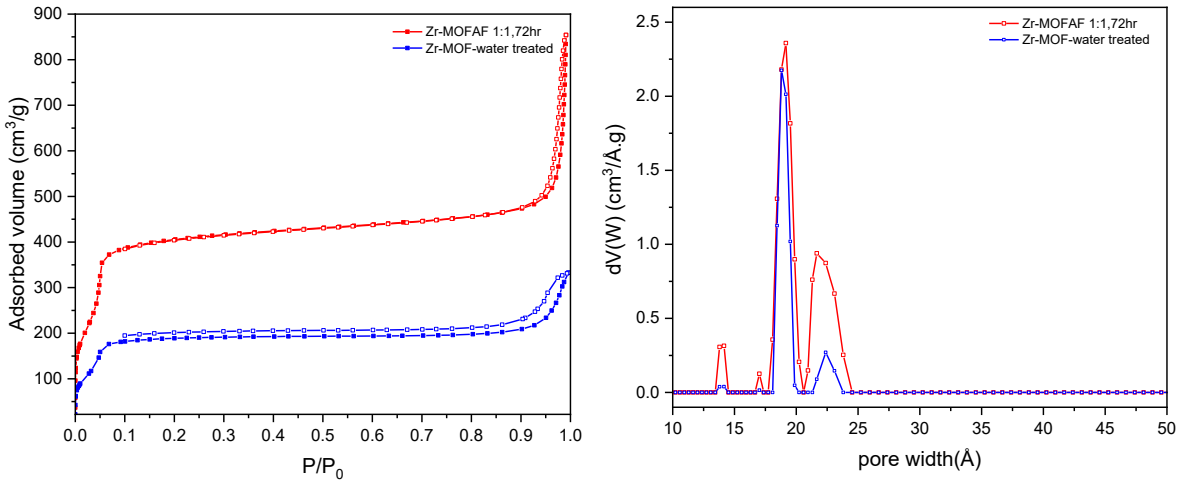

(a) *(b)*

Figure 7.3: Zr-MOFAF 1:1,72hr with its corresponding water treated sample (a)N2 Adsorption-Desorption isotherms (b)Pore size distribution

N_2 adsorption isotherms of the water-treated sample exhibit the characteristics of isotherms as a combination between type I and type IV isotherms formulating the presence of

mesoporous and microporous textures. The total volume adsorbed for a relative pressure below 0.1 corresponds to monolayer coverage in the microporous region. The curve then follows almost a plateau in the volume adsorbed until reaching a relative pressure of P/P_0=0.8 which indicates that no adsorbed volume was registered in some mesoporous regions. A small increase in the adsorbed volume followed by a noticeable hysteresis is recorded for a relative pressure above 0.8 which can be attributed to nitrogen filling in ink-bottled shape mesopores.

Table 7.2: Data obtained from N2 isotherms

Sample code	BET(m^2/g)	Total pore volume(cm^3/g)	Microporous area(m^2/g)	Microporous volume(cm^3/g)	Langmuir Area (m^2/g)
Zr-MOF-water treated	728.95	0.4941	505.5	0.1992	854.6
Zr-MOFAF 1:1,72hr	1619	1.321	897.395	0.367984	1977

In Table 7.2, it can be shown in drop in the reported BET and Langmuir area almost to half the non-treated sample Zr-MOFAF 1:1,72hr, which is also confirmed by the lower nitrogen uptake and decrease in peaks' intensities shown in Figure 7.3.

Overall, the water-treated sample shows a conserved crystallinity even if the decrease in surface area can be explained following two possibilities:

(1) Higher temperature degassing to be applied to remove water guest molecules.

(2) Collapse along specific planes with the same overall structure.

Conclusion

In this thesis we succeeded in the synthesis of a well-developed MOF 808 with chemical and physical properties matching the ones reported in literature following more optimized paths by decreasing the temperature and duration of the synthesis. It was also shown that samples synthesized with formic acid show much developed characteristics than samples synthesized with acetic acid; the use of acetic acid in the synthesis didn't show any interest in the development of the MOF, as it was lacking most of the its properties. $ZrOCl_2.8H_2O$ shows to be the ideal precursor to use instead of $ZrCl_4$ when combined with formic acid. Moreover, different molar ratios didn't show significant changes on the chemical-physical properties, allowing to decrease the amount of used reagents for a more sustainable synthesis protocol. In addition, the developed MOF show to be stable in water and acid, which are the two most by-products that are found in biomass reactions, which increases its interest in further catalytic application due to its structural- collapse resistance. The catalytic application on the promising MOF meet our expectation where the formation of Methyl Levulinate show much higher yield than conventional synthesis approaches that use biomass sugars, with much lower energy consumption.

References

1. Https://Www.Nationalgeographic.Com/Environment/Article/Greenhouse-Gases.
2. Wu, G.; Shen, C.; Liu, S.; Huang, Y.; Zhang, S.; Zhang, H. Research Progress on the Preparation and Application of Biomass Derived Methyl Levulinate. Green Chem. 2021, 23, 9254–9282, doi:10.1039/D1GC03474J.
3. Bioenergy Basics Available online: https://www.energy.gov/eere/bioenergy/bioenergy-basics (accessed on 20 May 2022).
4. T. Adeleye, A.; Louis, H.; U. Akakuru, O.; Joseph, I.; C. Enudi, O.; P. Michael, D.; 1 Dalian Institute of Chemical Physics, Chinese Academy of Sciences, Dalian 116023, P. R. China; 2 CAS Key Laboratory for Nanosystem and Hierarchical Fabrication, CAS Centre for Excellence in Nanoscience, National Centre for Nanoscience and Technology, University of Chinese Academy of Sciences, Beijing, China; 3 Ningbo Institute of Materials Technology and Engineering, Chinese Academy of Sciences, Zhejiang, China; 4 Department of Pure and Applied Chemistry, Faculty of Physical Sciences, University of Calabar, Calabar, Nigeria; et al. A Review on the Conversion of Levulinic Acid and Its Esters to Various Useful Chemicals. AIMS Energy 2019, 7, 165–185, doi:10.3934/energy.2019.2.165.
5. Shinde, S.H.; Hengne, A.; Rode, C.V. Lignocellulose-Derived Platform Molecules. In Biomass, Biofuels, Biochemicals; Elsevier, 2020; pp. 1–31 ISBN 978-0-444-64307-0.
6. Herbst, A.; Janiak, C. MOF Catalysts in Biomass Upgrading towards Value-Added Fine Chemicals. CrystEngComm 2017, 19, 4092–4117, doi:10.1039/C6CE01782G.
7. Signoretto, M.; Taghavi, S.; Ghedini, E.; Menegazzo, F. Catalytic Production of Levulinic Acid (LA) from Actual Biomass. Molecules 2019, 24, 2760, doi:10.3390/molecules24152760.
8. Cirujano, F.G.; Corma, A.; Llabrés i Xamena, F.X. Conversion of Levulinic Acid into Chemicals: Synthesis of Biomass Derived Levulinate Esters over Zr-Containing MOFs. Chemical Engineering Science 2015, 124, 52–60, doi:10.1016/j.ces.2014.09.047.
9. Kumaravel, S.; Thiripuranthagan, S.; Radhakrishnan, R.; Erusappan, E.; Durai, M.; Devarajan, A.; Mukannan, A. Liquid Phase Esterification of Levulinic Acid into Ethyl Levulinate Over Sulphobenzylated Nanoporous Al-SBA-15 Catalyst. j nanosci nanotechnol 2019, 19, 6965–6977, doi:10.1166/jnn.2019.16637.
10. Russo, V.; Tesser, R.; Rossano, C.; Cogliano, T.; Vitiello, R.; Leveneur, S.; Di Serio, M. Kinetic Study of Amberlite IR120 Catalyzed Acid Esterification of Levulinic Acid with Ethanol: From Batch to Continuous Operation. Chemical Engineering Journal 2020, 401, 126126, doi:10.1016/j.cej.2020.126126.
11. Fang, R.; Dhakshinamoorthy, A.; Li, Y.; Garcia, H. Metal Organic Frameworks for Biomass Conversion. Chem. Soc. Rev. 2020, 49, 3638–3687, doi:10.1039/D0CS00070A.
12. Bozell, J.J.; Moens, L.; Elliott, D.C.; Wang, Y.; Neuenscwander, G.G.; Fitzpatrick, S.W.; Bilski, R.J.; Jarnefeld, J.L. Production of Levulinic Acid and Use as a Platform Chemical for Derived Products. Resources, Conservation and Recycling 2000, 28, 227–239, doi:10.1016/S0921-3449(99)00047-6.

13. Qin, Y.; Guo, J.; Zhao, M. Metal–Organic Framework-Based Solid Acid Materials for Biomass Upgrade. Trans. Tianjin Univ. 2021, 27, 434–449, doi:10.1007/s12209-021-00298-4.
14. Isaeva, V.I.; Nefedov, O.M.; Kustov, L.M. Metal–Organic Frameworks-Based Catalysts for Biomass Processing. Catalysts 2018, 8, 368, doi:10.3390/catal8090368.
15. Siméant, J.; Pommerolle, M.-E.; Sommier, I. Zeolites and MOFs? 2022, 13.
16. Sud, D.; Kaur, G. A Comprehensive Review on Synthetic Approaches for Metal-Organic Frameworks: From Traditional Solvothermal to Greener Protocols. Polyhedron 2021, 193, 114897, doi:10.1016/j.poly.2020.114897.
17. Yaghi, O.M.; Kalmutzki, M.J.; Diercks, C.S. Introduction to Reticular Chemistry: Metal-Organic Frameworks and Covalent Organic Frameworks; 1st ed.; Wiley, 2019; ISBN 978-3-527-34502-1.
18. Alshammari, A.; Jiang, Z.; Cordova, K.E. Metal Organic Frameworks as Emerging Photocatalysts. In Semiconductor Photocatalysis - Materials, Mechanisms and Applications; Cao, W., Ed.; InTech, 2016 ISBN 978-953-51-2484-9.
19. Eyley, J. Gas Sorption and Binding Site Studies in Metal Organic Frameworks. 225.
20. Delasalle, J. University of Warwick Institutional Repository: Http://Go. 364.
21. Marshall, R.J. Synthesis, Characterisation and Postsynthetic Modification of Zirconium and Hafnium Metal-Organic Frameworks. 280.
22. Butova, V.V.; Soldatov, M.A.; Guda, A.A.; Lomachenko, K.A.; Lamberti, C. Metal-Organic Frameworks: Structure, Properties, Methods of Synthesis and Characterization. Russ. Chem. Rev. 2016, 85, 280, doi:10.1070/RCR4554.
23. Newton Augustus, E.; Nimibofa, A.; Azibaola Kesiye, I.; Donbebe, W. Metal-Organic Frameworks as Novel Adsorbents: A Preview. ENV 2017, 5, 61–67, doi:10.12691/env-5-2-5.
24. Vakiti, R.K. Hydro/Solvothermal Synthesis, Structures and Properties of Metal-Organic Frameworks Based on S-Block Metals. 91.
25. Dzumbira, W.; Ali, N.; Duanmu, C.; Yang, Y.; Khan, A.; Ali, F.; Bilal, M.; Aleya, L.; Iqbal, H.M.N. Separation and Remediation of Environmental Pollutants Using Metal–Organic Framework-Based Tailored Materials. Environ Sci Pollut Res 2022, 29, 4822–4842, doi:10.1007/s11356-021-17446-x.
26. Dhaka, S.; Kumar, R.; Deep, A.; Kurade, M.B.; Ji, S.-W.; Jeon, B.-H. Metal–Organic Frameworks (MOFs) for the Removal of Emerging Contaminants from Aquatic Environments. Coordination Chemistry Reviews 2019, 380, 330–352, doi:10.1016/j.ccr.2018.10.003.
27. Jiao, L.; Seow, J.Y.R.; Skinner, W.S.; Wang, Z.U.; Jiang, H.-L. Metal–Organic Frameworks: Structures and Functional Applications. Materials Today 2019, 27, 43–68, doi:10.1016/j.mattod.2018.10.038.
28. Bavykina, A.; Kolobov, N.; Khan, I.S.; Bau, J.A.; Ramirez, A.; Gascon, J. Metal–Organic Frameworks in Heterogeneous Catalysis: Recent Progress, New Trends, and Future Perspectives. Chem. Rev. 2020, 120, 8468–8535, doi:10.1021/acs.chemrev.9b00685.
29. MSci, R.A.H. Metal-Organic Frameworks: Towards Greener Synthesis. 378.
30. Bedia, J.; Muelas-Ramos, V.; Peñas-Garzón, M.; Gómez-Avilés, A.; Rodríguez, J.; Belver, C. A Review on the Synthesis and Characterization of Metal Organic Frameworks for Photocatalytic Water Purification. Catalysts 2019, 9, 52, doi:10.3390/catal9010052.

31. Yan, X.; Wang, K.; Xu, X.; Wang, S.; Ning, Q.; Xiao, W.; Zhang, N.; Chen, Z.; Chen, C. Brønsted Basicity in Metal–Organic Framework-808 and Its Application in Base-Free Catalysis. Inorg. Chem. 2018, 57, 8033–8036, doi:10.1021/acs.inorgchem.8b01044.
32. Https://Www.Jove.Com/It/v/10446/x-Ray-Diffraction.
33. Norbert Broll. Caractérisation de Solides Cristallisés Par Diffraction X. Page 21, 1996. In.
34. Rabiei, M.; Palevicius, A.; Monshi, A.; Nasiri, S.; Vilkauskas, A.; Janusas, G. Comparing Methods for Calculating Nano Crystal Size of Natural Hydroxyapatite Using X-Ray Diffraction. Nanomaterials 2020, 10, 1627, doi:10.3390/nano10091627.
35. Rebuffi, L.; Sánchez del Río, M.; Busetto, E.; Scardi, P. Understanding the Instrumental Profile of Synchrotron Radiation X-Ray Powder Diffraction Beamlines. J Synchrotron Rad 2017, 24, 622–635, doi:10.1107/S1600577517005434.
36. Can J Chem Eng - 2020 - Khan - Experimental Methods in Chemical Engineering X-ray Diffraction Spectroscopy XRD.Pdf.
37. Holder, C.F.; Schaak, R.E. Tutorial on Powder X-Ray Diffraction for Characterizing Nanoscale Materials. ACS Nano 2019, 13, 7359–7365, doi:10.1021/acsnano.9b05157.
38. Bertier, P.; Schweinar, K.; Stanjek, H.; Ghanizadeh, A.; Clarkson, C.R.; Busch, A.; Kampman, N.; Prinz, D.; Amann-Hildebrand, A.; Krooss, B.M.; et al. On the Use and Abuse of N2 Physisorption for the Characterization of the Pore Structure of Shales. In; 2016; pp. 151–161.
39. Https://Www.Particletechlabs.Com/Analytical-Testing/Gas-Adsorption-and-Porosimetry/Bet-Specific-Surface-Area.
40. Wu, H. Physical and Thermal Properties of Zirconium Tungstate Nanoparticles with Different Morphologies from Hydrothermal Synthesis.; 2012.
41. Sdanghi, G.; Canevesi, R.L.S.; Celzard, A.; Thommes, M.; Fierro, V. Characterization of Carbon Materials for Hydrogen Storage and Compression. 2020, 28.
42. Fundamentals of the Adsorption Theory. In Partition and Adsorption of Organic Contaminants in Environmental Systems, Pages 39–52. John Wiley & Sons, Inc., Hoboken, NJ, USA, May 2003.;
43. Thommes, M.; Kaneko, K.; Neimark, A.V.; Olivier, J.P.; Rodriguez-Reinoso, F.; Rouquerol, J.; Sing, K.S.W. Physisorption of Gases, with Special Reference to the Evaluation of Surface Area and Pore Size Distribution (IUPAC Technical Report). Pure and Applied Chemistry 2015, 87, 1051–1069, doi:10.1515/pac-2014-1117.
44. Loganathan, S.; Valapa, R.B.; Mishra, R.K.; Pugazhenthi, G.; Thomas, S. Thermogravimetric Analysis for Characterization of Nanomaterials. In Thermal and Rheological Measurement Techniques for Nanomaterials Characterization; Elsevier, 2017; pp. 67–108 ISBN 978-0-323-46139-9.
45. Howarth, A.J.; Peters, A.W.; Vermeulen, N.A.; Wang, T.C.; Hupp, J.T.; Farha, O.K. Best Practices for the Synthesis, Activation, and Characterization of Metal–Organic Frameworks. Chem. Mater. 2017, 29, 26–39, doi:10.1021/acs.chemmater.6b02626.
46. Minkiewicz, J. Solvothermal Stability Studies of Porous Inorganic and Metal-Organic Materials. 196.
47. Https://Www.Nanalysis.Com/Nmready-Blog/2019/6/26/What-Is-Nmr-Spectrography-and-How-Does-It-Work.
48. Https://Chem.Libretexts.Org/Bookshelves/Physical_and_Theoretical_Chemistry_Textbook_Maps/Supplemental_Modules_(Physical_and_Theoretical_Chemistry)/Spectrosc

opy/Magnetic_Resonance_Spectroscopies/Nuclear_Magnetic_Resonance/Nuclear_Magnetic_Resonance_II.
49. Cao, R.; Liu, X.; Liu, Y.; Zhai, X.; Cao, T.; Wang, A.; Qiu, J. Applications of Nuclear Magnetic Resonance Spectroscopy to the Evaluation of Complex Food Constituents. Food Chemistry 2021, 342, 128258, doi:10.1016/j.foodchem.2020.128258.
50. Falconer, J.L.; Schwarz, J.A. Temperature-Programmed Desorption and Reaction: Applications to Supported Catalysts. Catalysis Reviews 1983, 25, 141–227, doi:10.1080/01614948308079666.
51. Trujillo, C.-A.; Ramírez-Marquez, N.-T.; Valencia-Rios, J.-S. An Affordable Ammonia Temperature-Programmed Desorption Equipment and Its Calibration Using the Thermal Decomposition of Ammonium Dihydrogen Phosphate. Thermochimica Acta 2020, 689, 178651, doi:10.1016/j.tca.2020.178651.
52. Https://Serc.Carleton.Edu/Research_education/Geochemsheets/Techniques/SEM.Html.
53. Https://Www.Scimed.Co.Uk/Education/Sem-Scanning-Electron-Microscopy/.
54. Di Menno Di Bucchianico, D.; Wang, Y.; Buvat, J.-C.; Pan, Y.; Casson Moreno, V.; Leveneur, S. Production of Levulinic Acid and Alkyl Levulinates: A Process Insight. Green Chem. 2022, 24, 614–646, doi:10.1039/D1GC02457D.
55. Démolis, A.; Essayem, N.; Rataboul, F. Synthesis and Applications of Alkyl Levulinates. ACS Sustainable Chem. Eng. 2014, 2, 1338–1352, doi:10.1021/sc500082n.
56. X. He, Shengwuzhi Huaxue Gongcheng, 2015, 49, 65–65.
57. D. Ding, J. Xi, J. Wang, X. Liu, G. Lu and Y. Wang, Green Chem., 2015, 17, 4037–4044.
58. Y. Zhang, B. Yang and W. Dong, Dangdai Huagong, 2020, 49, 1596–1600.
59. S. Zeng, L. Lin and L. Peng, Xiandai Shipin Keji, 2011, 27, 783–787.
60. Raspolli Galletti, A.M.; Antonetti, C.; Fulignati, S.; Licursi, D. Direct Alcoholysis of Carbohydrate Precursors and Real Cellulosic Biomasses to Alkyl Levulinates: A Critical Review. Catalysts 2020, 10, 1221, doi:10.3390/catal10101221.
61. Plessers, E.; Fu, G.; Tan, C.; De Vos, D.; Roeffaers, M. Zr-Based MOF-808 as Meerwein–Ponndorf–Verley Reduction Catalyst for Challenging Carbonyl Compounds. Catalysts 2016, 6, 104, doi:10.3390/catal6070104.
62. Zheng, H.-Q.; Zeng, Y.-N.; Chen, J.; Lin, R.-G.; Zhuang, W.-E.; Cao, R.; Lin, Z.-J. Zr-Based Metal–Organic Frameworks with Intrinsic Peroxidase-Like Activity for Ultradeep Oxidative Desulfurization: Mechanism of H_2O_2 Decomposition. Inorg. Chem. 2019, 58, 6983–6992, doi:10.1021/acs.inorgchem.9b00604.
63. Pascanu, V.; González Miera, G.; Inge, A.K.; Martín-Matute, B. Metal–Organic Frameworks as Catalysts for Organic Synthesis: A Critical Perspective. J. Am. Chem. Soc. 2019, 141, 7223–7234, doi:10.1021/jacs.9b00733.
64. Https://Chem.Libretexts.Org/Bookshelves/General_Chemistry/Map%3A_Chemistry_-_The_Central_Science_(Brown_et_al.)/14%3A_Chemical_Kinetics/14.01%3A_Factors_that_Affect_Reaction_Rates.
65. Https://Pubs.Rsc.Org/En/Content/Articlelanding/2018/Cy/C7cy02462b.
66. Feng, J.; Zhong, Y.; Xie, M.; Li, M.; Jiang, S. Using MOF-808 as a Promising Support to Immobilize Ru for Selective Hydrogenation of Levulinic Acid to γ-Valerolactone. Catal Lett 2021, 151, 86–94, doi:10.1007/s10562-020-03277-x.
67. Walton, I.M.; Cox, J.M.; Benson, C.A.; Patel, D. (Dan) G.; Chen, Y.-S.; Benedict, J.B. The Role of Atropisomers on the Photo-Reactivity and Fatigue of Diarylethene-Based Metal–Organic Frameworks. New J. Chem. 2016, 40, 101–106, doi:10.1039/C5NJ01718A.

68. Https://Www.Anton-Paar.Com/Corp-En/Services-Support/Document-Finder/Application-Reports/Micropore-Area-and-Volume-by-the-t-Plot-Method/.
69. Zhou, Y.; Gao, Q.; Zhang, L.; Zhou, Y.; Zhong, Y.; Yu, J.; Liu, J.; Huang, C.; Wang, Y. Combining Two into One: A Dual-Function $H_5PV_2Mo_{10}O_{40}$@MOF-808 Composite as a Versatile Decontaminant for Sulfur Mustard and Soman. Inorg. Chem. 2020, 59, 11595–11605, doi:10.1021/acs.inorgchem.0c01392.
70. Mukhtar, A.; Mellon, N.; Saqib, S.; Lee, S.-P.; Bustam, M.A. Extension of BET Theory to CO2 Adsorption Isotherms for Ultra-Microporosity of Covalent Organic Polymers. SN Appl. Sci. 2020, 2, 1232, doi:10.1007/s42452-020-2968-9.
71. Ardila-Suárez, C.; Díaz-Lasprilla, A.M.; Díaz-Vaca, L.A.; Balbuena, P.B.; Baldovino-Medrano, V.G.; Ramírez-Caballero, G.E. Synthesis, Characterization, and Post-Synthetic Modification of a Micro/Mesoporous Zirconium–Tricarboxylate Metal–Organic Framework: Towards the Addition of Acid Active Sites. CrystEngComm 2019, 21, 3014–3030, doi:10.1039/C9CE00218A.
72. Ardila-Suárez, C.; Molina V., D.R.; Alem, H.; Baldovino Medrano, V.G.; Ramírez-Caballero, G.E. Synthesis of Ordered Microporous/Macroporous MOF-808 through Modulator-Induced Defect Formation, and Surfactant Self-Assembly Strategies; Chemistry, 2019;
73. Hu, Z.; Kundu, T.; Wang, Y.; Sun, Y.; Zeng, K.; Zhao, D. Modulated Hydrothermal Synthesis of Highly Stable MOF-808(Hf) for Methane Storage. ACS Sustainable Chem. Eng. 2020, 8, 17042–17053, doi:10.1021/acssuschemeng.0c04486.
74. Hardian, R.; Dissegna, S.; Ullrich, A.; Llewellyn, P.L.; Coulet, M.; Fischer, R.A. Tuning the Properties of MOF-808 via Defect Engineering and Metal Nanoparticle Encapsulation. Chem. Eur. J. 2021, 27, 6804–6814, doi:10.1002/chem.202005050.
75. Taddei, M.; Dau, P.V.; Cohen, S.M.; Ranocchiari, M.; van Bokhoven, J.A.; Costantino, F.; Sabatini, S.; Vivani, R. Efficient Microwave Assisted Synthesis of Metal–Organic Framework UiO-66: Optimization and Scale Up. Dalton Trans. 2015, 44, 14019–14026, doi:10.1039/C5DT01838B.
76. Dai, S.; Simms, C.; Dovgaliuk, I.; Patriarche, G.; Tissot, A.; Parac-Vogt, T.N.; Serre, C. Monodispersed MOF-808 Nanocrystals Synthesized via a Scalable Room-Temperature Approach for Efficient Heterogeneous Peptide Bond Hydrolysis. Chem. Mater. 2021, 33, 7057–7066, doi:10.1021/acs.chemmater.1c02174.
77. Sultan, M.; Miyazaki, T.; Koyama, S. Optimization of Adsorption Isotherm Types for Desiccant Air-Conditioning Applications. Renewable Energy 2018, 121, 441–450, doi:10.1016/j.renene.2018.01.045.
78. Xuan, K.; Pu, Y.; Li, F.; Luo, J.; Zhao, N.; Xiao, F. Metal-Organic Frameworks MOF-808-X as Highly Efficient Catalysts for Direct Synthesis of Dimethyl Carbonate from CO2 and Methanol. Chinese Journal of Catalysis 2019, 40, 553–566, doi:10.1016/S1872-2067(19)63291-2.
79. Chen, Y.; Zhang, X.; Mian, M.R.; Son, F.A.; Zhang, K.; Cao, R.; Chen, Z.; Lee, S.-J.; Idrees, K.B.; Goetjen, T.A.; et al. Structural Diversity of Zirconium Metal–Organic Frameworks and Effect on Adsorption of Toxic Chemicals. J. Am. Chem. Soc. 2020, 142, 21428–21438, doi:10.1021/jacs.0c10400.
80. Shan, B.; McIntyre, S.M.; Armstrong, M.R.; Shen, Y.; Mu, B. Investigation of Missing-Cluster Defects in UiO-66 and Ferrocene Deposition into Defect-Induced Cavities. Ind. Eng. Chem. Res. 2018, 57, 14233–14241, doi:10.1021/acs.iecr.8b03516.